Available online at www.sciencedirect.com

ScienceDirect

Journal of Terramechanics 73 (2017) 73–93

Journal of Terramechanics

www.elsevier.com/locate/jterra

Relating geologic units and mobility system kinematics contributing to Curiosity wheel damage at Gale Crater, Mars

R.E. Arvidson [a,*], P. DeGrosse Jr [b], J.P. Grotzinger [c], M.C. Heverly [b], J. Shechet [c], S.J. Moreland [b], M.A. Newby [b], N. Stein [c], A.C. Steffy [b], F. Zhou [a], A.M. Zastrow [a], A.R. Vasavada [b], A.A. Fraeman [b], E.K. Stilly [b]

[a] McDonnell Center for the Space Sciences, Department of Earth and Planetary Sciences, Washington University in St. Louis, St. Louis, MO 63130, USA
[b] Jet Propulsion Laboratory, California Institute of Technology, Pasadena, CA 91109, USA
[c] Division of Geological and Planetary Sciences, California Institute of Technology, Pasadena, CA 91125, USA

Received 17 November 2016; accepted 5 March 2017
Available online 12 April 2017

Abstract

Curiosity landed on plains to the north of Mount Sharp in August 2012. By June 2016 the rover had traversed 12.9 km to the southwest, encountering extensive strata that were deposited in a fluvial-deltaic-lacustrine system. Initial drives across sharp sandstone outcrops initiated an unacceptably high rate of punctures and cracks in the thin aluminum wheel skin structures. Initial damage was found to be related to the drive control mode of the six wheel drive actuators and the kinematics of the rocker-bogie suspension. Wheels leading a suspension pivot were forced onto sharp, immobile surfaces by the other wheels as they maintained their commanded angular velocities. Wheel damage mechanisms such as geometry-induced stress concentration cracking and low-cycle fatigue were then exacerbated. A geomorphic map was generated to assist in planning traverses that would minimize further wheel damage. A steady increase in punctures and cracks between landing and June 2016 was due in part because of drives across the sharp sandstone outcrops that could not be avoided. Wheel lifetime estimates show that with careful path planning the wheels will be operational for an additional ten kilometers or more, allowing the rover to reach key strata exposed on the slopes of Mount Sharp.

Keywords: Mars rovers; Curiosity rover; Ackerman arcs

1. Introduction

The NASA Mars Science Laboratory Curiosity rover landed on the northern plains of Gale Crater at the base of Mount Sharp (formally known as Aeolis Mons) on August 6, 2012 (Grotzinger et al., 2012; Vasavada et al., 2014) (Figs. 1 and 2). By June 1, 2016 Curiosity had traversed 12.9 km during its first 1358 sols (Mars days) on the surface, using its remote sensing and in-situ instruments to show that strata encountered consist of sedimentary rocks deposited in an ancient fluvial-deltaic-lacustrine sys-

Abbreviations: NASA, National Aeronautics and Space Administration; Hazcams, hazard avoidance cameras; Navcam, navigation camera; IMU, inertial measurement units; Mastcam, mast camera; MAHLI, Mars Hand Lens Imager; HiRISE, High Resolution Imaging Science Experiment; THEMIS, Thermal Emission Imaging System; VIS, visible

* Corresponding author.
E-mail address: arvidson@wunder.wustl.edu (R.E. Arvidson).

http://dx.doi.org/10.1016/j.jterra.2017.03.001
0022-4898/

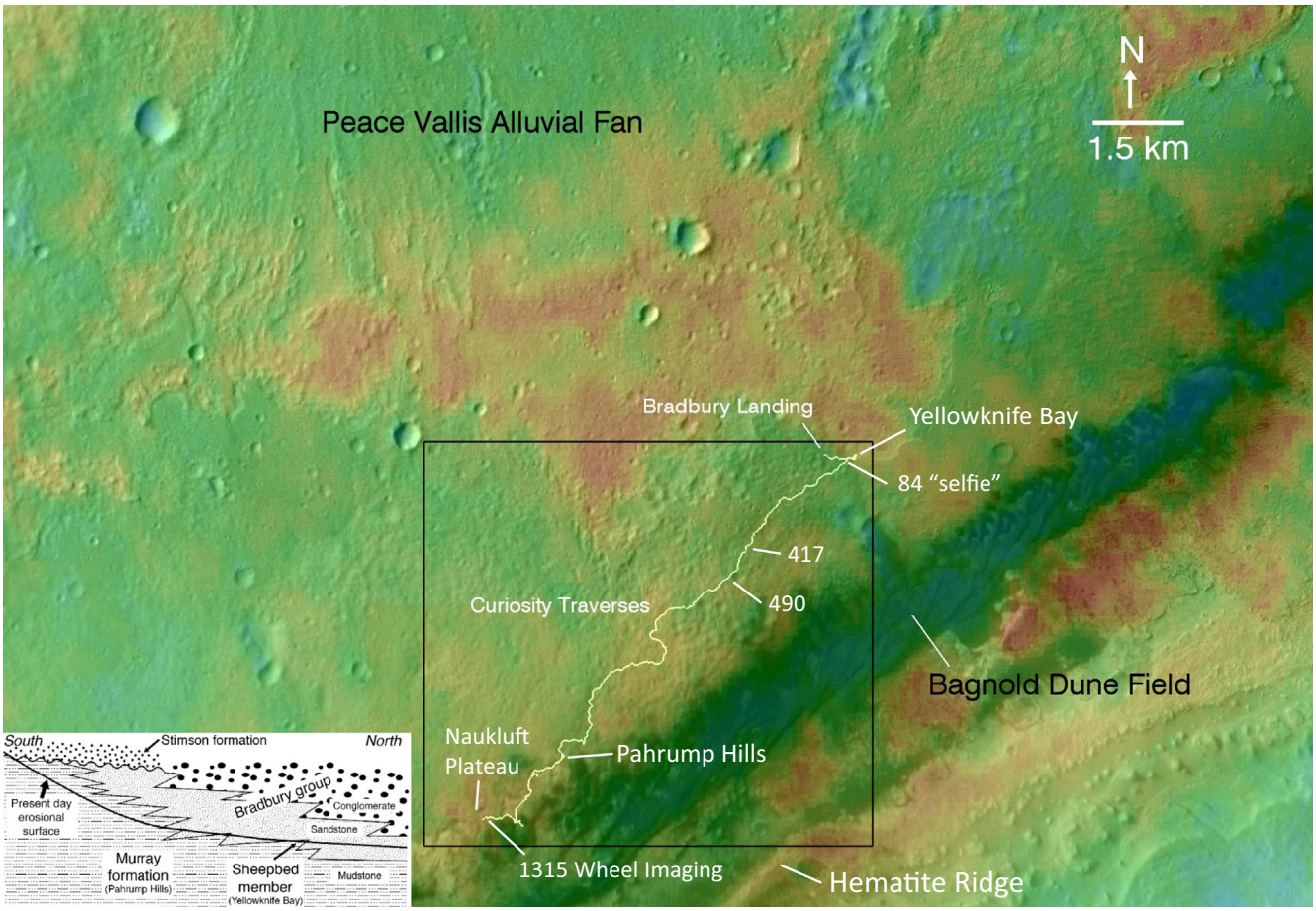

Fig. 1. **Orbital view of Curiosity's paths.** THEMIS VIS mosaic (Christensen et al., 2004) color coded with thermal inertia values and covering Gale Crater plains to the north of Mount Sharp, dissected terrains on the lower slopes of Mount Sharp, and the Bagnold dune field, with Curiosity's traverses overlain. Intent is to show smooth plains transitioning into highly eroded terrains exposing fluvial-deltaic-lacustrine deposits. The smooth plains are characterized by relatively low thermal inertias whereas the dissected underlying deposits have higher thermal inertias associated with greater bedrock exposures. View on lower left shows a north to south cross section through the fluvial-deltaic-lacustrine deposits traversed by the rover. Black box delineates area shown in detail in Fig. 8. Traverses are shown from Bradbury landing through the position on sol 1357, when the rover was at the edge of the Naukluft Plateau. MAHLI-based wheel imaging was acquired periodically and the last one acquired during the period reviewed by this paper was on sol 1315 (Fig. 19). On sol 84 Curiosity was commanded to acquire a "selfie" of itself using the arm-based MAHLI instrument (see Fig. 2). Navcam-based mosaics for sols 417 and 490 are shown in Fig. 3 and one for the Pahrump Hills region is shown in Fig. 22. Blue colors correspond to low and red to high thermal inertia values, with a dynamic range of ~200–550 J m^{-2} K^{-1} $s^{0.5}$. (For interpretation of the references to colour in this figure legend, the reader is referred to the web version of this article.)

tem (Williams et al., 2013; Grotzinger et al., 2015). After traversing ~12.9 km Curiosity was poised at the edge of the Naukluft Plateau on the lower slopes of Mount Sharp (Fig. 1), ready to continue its ascent and characterization of the exposed strata.

During the first ~4 km of traverses the rover mainly crossed plains surfaces, with a relatively thin, dominantly sand to clay-sized regolith cover over bedrock, with rocks of a variety of sizes dispersed across the landscape (Arvidson et al., 2014). For reference, regolith on Mars is defined as loose or loosely consolidated particulate material generated by impact, physical and chemical weathering of local bedrock, and the addition of wind-blown granule, sand, silt, and clay-size particles (Moore, 1987; Arvidson et al., 1989). As Curiosity continued traversing to the southwest on the way to Mount Sharp the terrain transitioned to exposures within the plains of well-indurated sandstone outcrops shaped into immobile, sharp surfaces by fracturing and wind erosion. This terrain then transitioned to sandstone-capped plateaus with intervening valleys formed as wind erosion carved into the plains and exposed underlying bedrock (Fig. 1). The well-indurated fluvial and deltaic sandstones resisted erosion and formed rough, capping outcrops. Driving over these sharp sandstones on the plains initiated several damage mechanisms, including an unacceptably high rate of punctures and cracks in the 0.75 mm thick aluminum wheel surfaces, thereby initiating efforts designed to understand the damage mechanisms and mitigate further damage during subsequent drives. For reference, punctures are defined as single-event free-field (inter-grouser) wheel skin penetrations. Cracks and low load punctures are a more complex dam-

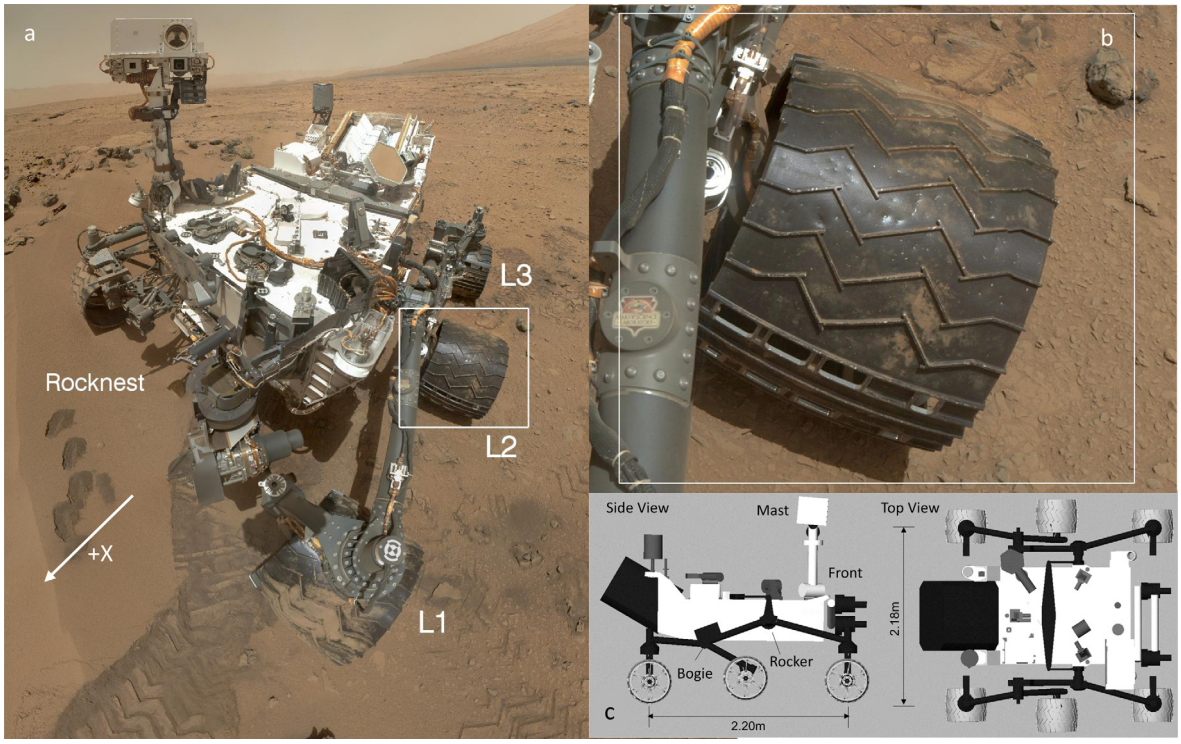

Fig. 2. **Mosaic of Curiosity taken on sol 84.** (a) MAHLI-based mosaic of Curiosity taken on sol 84 when the rover was located in the boulder-strewn sand drift called Rocknest near Yellowknife Bay. This "selfie" was acquired by positioning MAHLI at various locations for imaging using the robotic arm. (b) Close-up showing the relatively pristine nature of the left middle wheel (L2). Only dents can be seen with no tears or punctures. (c) Side and plan views of Curiosity to illustrate the rocker-bogie mobility system and the scale of the rover. MAHLI mosaic PIA20752 available on the NASA Photojournal. The $+X$ direction is shown and corresponds to driving in a forward direction.

age mode indicative of stress concentrations, low cycle fatigue (i.e., accumulated plastic deformation and associated micro-cracking), and additional extensions of original penetrations.

This paper focuses on the mechanics of initial free-field wheel punctures, geologic units traversed by the rover and their relationship to total wheel damage, their geomorphic expressions as wind eroded the deposits, and traverses designed to minimize additional wheel wear after initial damage was observed on the sharp sandstone outcrops. The period from touch-down at Bradbury Landing to traversing to the edge of the Naukluft Plateau (Fig. 1) will be covered because the traverses and terrains between these two localities both illustrate the relationships between terrains and wheel damage, and how drives were accomplished to minimize further wear.

2. The Curiosity rover and drive modes

Curiosity has a mass of 899 kg and employs six-wheel drive, with the front and rear wheels capable of steering about vertical axes using azimuthal actuators (Fig. 2). For clarity this paper will refer to the left front wheel as wheel L1, the left middle wheel as wheel L2, and the left rear wheel as wheel L3. Right side wheels are designated using the same nomenclature. Left and right sides are defined relative to the rover-based $+X$ coordinate, which extends outward from the front of the vehicle (Fig. 2). Specifically, right and left are defined relative to an observer located at the vehicle and looking toward the $+X$ direction. Curiosity has a free pivoting rocker-bogie suspension system on each side of the vehicle, with opposing rocker pivots connected by a differencing mechanism. The mobility system is designed to go over obstacles while maintaining low rover tilts, and evenly distributing the rover weight among the wheels (Bickler, 1988). Wheels are rigid and made of forged aluminum alloy, 0.5 m in diameter and 0.4 m wide, machined to 0.75 mm skin thickness, with integral 7.5 mm tall chevron-shaped external grousers to promote traction, and three integral internal formers to both stiffen the wheel and provide hard points to attach the spokes (Haggert and Waydo, 2008). The relatively thin skin was a consequence of the need to minimize the total mass of the vehicle, including the total mass of Curiosity's wheels and suspension system, which deployed during final descent as the Sky Crane lowered the vehicle to the ground on a 6.7 m long tether. In retrospect implementing the thin skin design was also a consequence of incomplete understanding of the reaction loads and resultant damage associated with driving over outcrops with sharp surfaces, i.e., the subject of this paper.

Wheel actuators were chosen for steering and driving purposes that provided torque values estimated to be several times higher than typically needed in order to achieve

an adequate torque margin. Drives on Mars are accomplished along Ackerman arcs of given radii of curvature using the left and right wheel 1 and wheel 3 steering actuators to set the path curvature, along with appropriate drive actuator angular velocities needed to maintain the commanded arcuate drive path. Autonomous navigation using body-mounted hazard avoidance stereo cameras (Front and Rear Hazcams) and mast-mounted Navcam stereo cameras (Maki et al., 2012) are used when needed to automatically detect and plan paths around large obstacles (Maimone et al., 2007). Visual odometry using periodic stereo imaging of the surrounding terrain taken by the mast-mounted Navcams (Maki et al., 2012) is also used when needed to determine actual drive distances and directions, which the rover can then use to correct path vectors relative to commanded values (Maimone et al., 2007). Drives can be commanded to: a. traverse to waypoints using only inertial measurement units (IMU) to keep on the correct heading, b. the addition of visual odometry to periodically update positions and headings, and stop if progress is poor, and c. the addition of autonomous hazard avoidance imaging to identify and command moves around non-traversable obstacles while still seeking commanded waypoints.

Engineering data recorded by Curiosity during its drives can be collected at rates varying from 2 to 64 Hz, and include downlinked time series of rover tilt vectors (using IMUs), rocker and bogie suspension angles, wheel rotations, and wheel actuator currents. In addition, stereo images are acquired using Hazcam and Navcam cameras at end of drive locations to help ground operators plan paths for subsequent drives. Drive distances/sol have ranged from several to approximately one hundred meters, depending on terrain complexity and traverse objectives. For reference, a sol is one Martian day, which is approximately 39 min longer than an Earth day.

3. Initial wheel damage and responses

The Sky Crane landing system placed Curiosity onto the plains to the north of Mount Sharp wheels down, with an impact velocity of ~0.6 m/s. Examination of the wheels and rocker-bogie suspension system after landing using the mast-mounted Mastcam (Malin et al., 2010) and Nav-

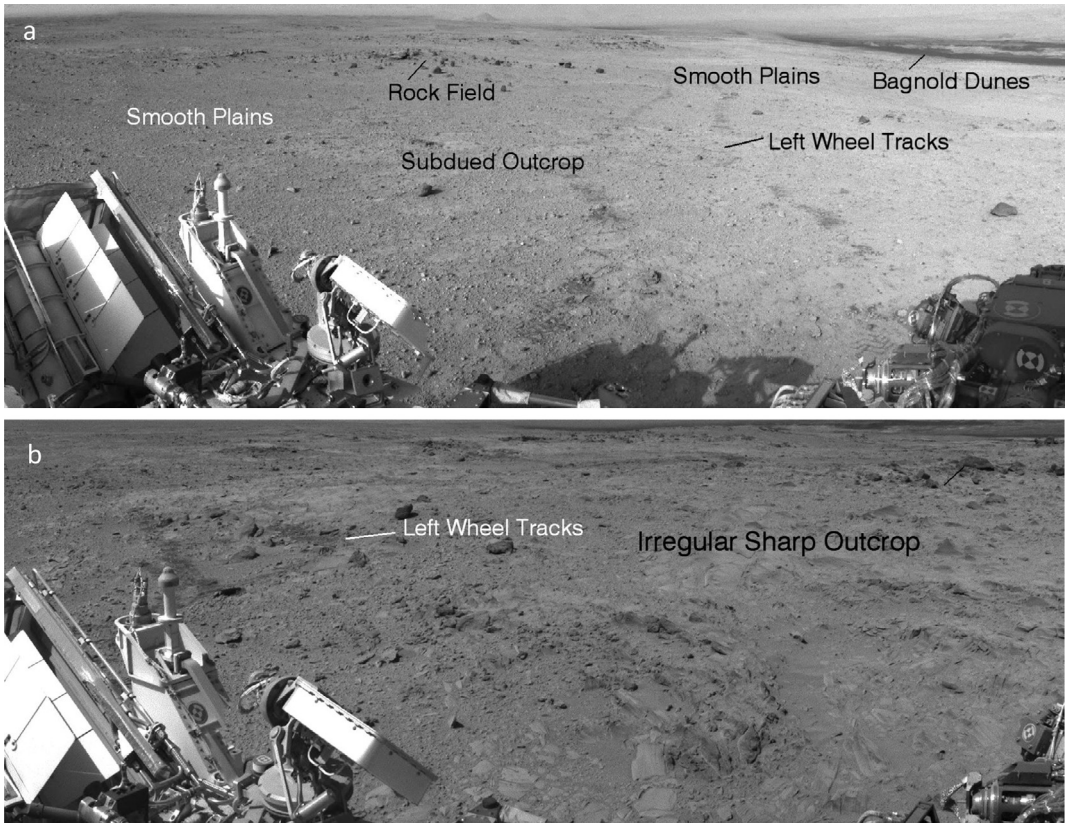

Fig. 3. **Navcam mosaics showing smooth plains and sharp sandstone outcrops.** (a) Navcam mosaic showing tracks associated with the sol 417 drive across smooth plains. Tracks are evident where darker regolith was exposed by the wheels. Relatively small rocks were rotated or pushed into the regolith by the wheels. (b) Traverse shown across irregular, sharp outcrops on sol 490. The left wheels traversed through sharp rocks and strewn boulders. The outcrop is composed of well-cemented sandstones that have been fractured and wind-eroded to immobile surfaces with some sharp edges. CX00417NL0180786F434526337VA.JPG is the source for (a) from the Curiosity Analyst Notebook (https://an.rsl.wustl.edu/msl/mslbrowser/default.aspx). Data for (b) are from CX00490NL0240408F440996169VA.JPG.

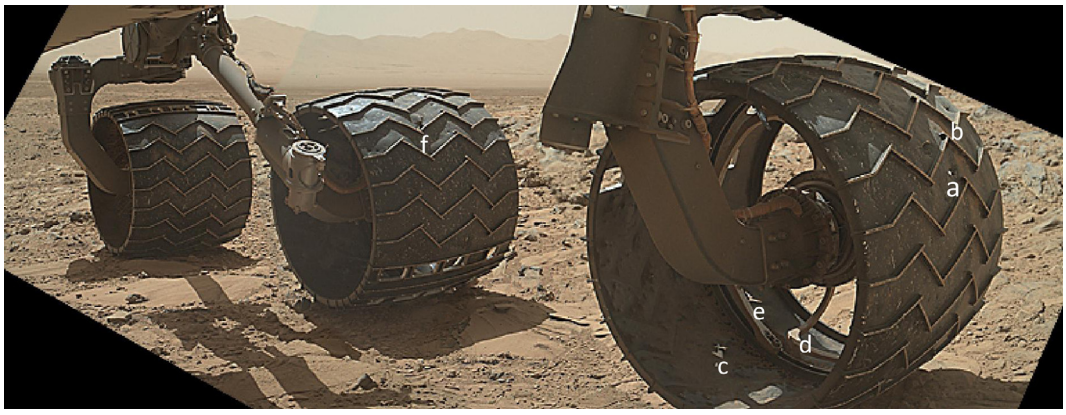

Fig. 4. **Mosaic of Curiosity left wheels taken on sol 488.** MAHLI-based mosaic showing the left wheels on sol 488 after crossing initial irregular sandstones that have been shaped by fracturing and wind into sharp surfaces. Letters labeled on wheels show individual punctures (denoted by letter a) and tears (remaining letters) for the front (L1) and middle (L2) wheels. None were found for the rear (L3) wheel. Image products 0488MH 000262000 0200500 E01_DRCL, 0488MH0002630000200498E01_DRCL, and 0488MH0002640000200496E01_DRCL used in generating the mosaic.

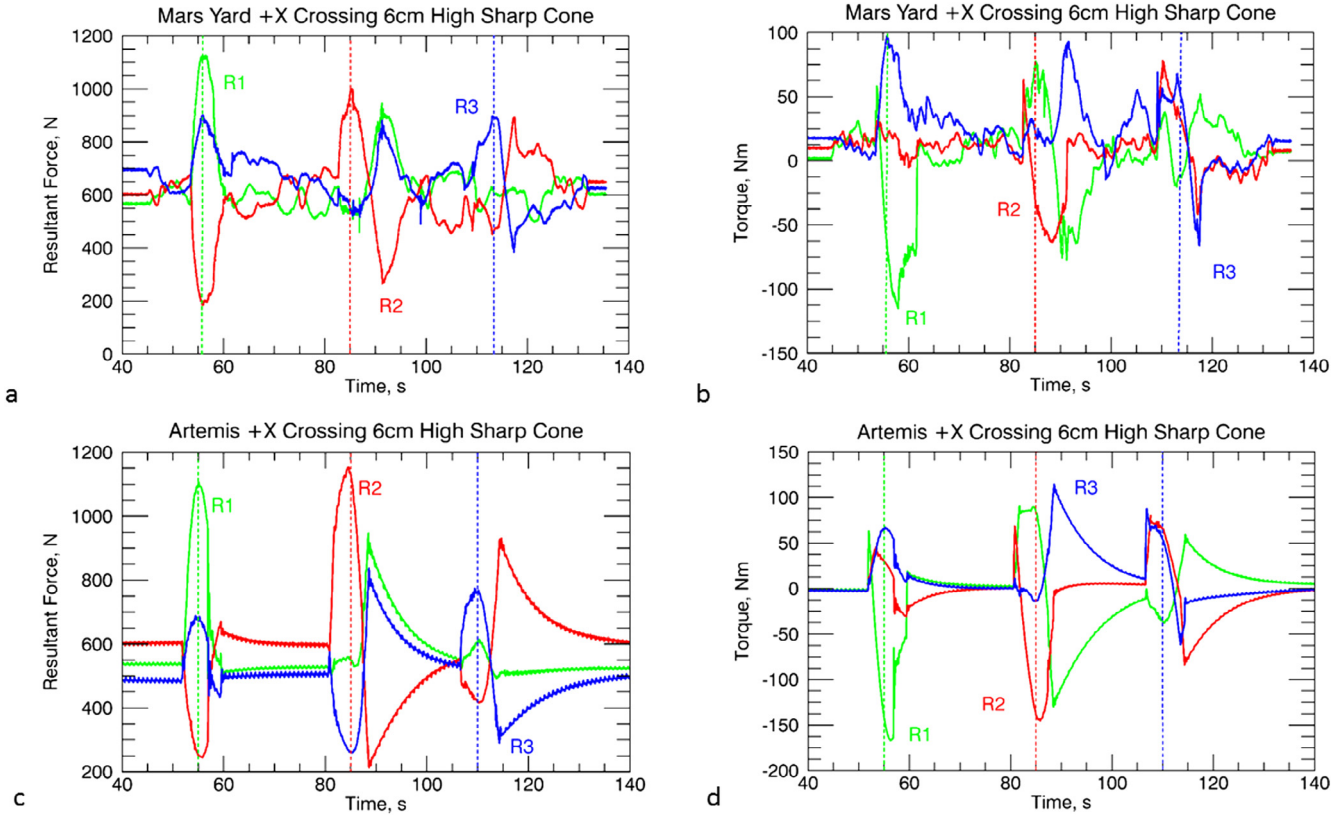

Fig. 5. **Resultant force as a function of time for Mars Yard and Artemis +*X* drive.** (a) Resultant forces as function of time are shown for instrumented right side wheels on the Scarecrow rover driving in the $+X$ direction (forward drive) over an immobile 6 cm high steel right circular cone with 60° sloping sides, simulating a sharp rock. (b) Plot of drive actuator torques for Scarecrow with positive torques for driving and negative torques for slowing down. (c) Resultant forces as function of time are shown for wheels for the Artemis model for Curiosity under Martian gravity driving over the immobile 6 cm high sharp cone. (d) Plot of drive actuator torques for the Artemis simulation with positive torques for driving and negative torques for slowing down. The trends in the plots are quite similar for Scarecrow and Artemis. Color-coded vertical dashed lines show cone crossings for the wheels. See text for detailed analysis of the forces and torques. (For interpretation of the references to colour in this figure legend, the reader is referred to the web version of this article.)

cam imaging system, the body-mounted Hazcams, together with the arm-mounted Mars Hand Lens Imager (MAHLI, Edgett et al., 2012), showed only slight wheel damage (crack in the L2 wheel) associated with the touchdown. After system check-out the rover was commanded to drive to nearby targets and then begin a set of traverses to the east (~500 m total distance) across the plains to Yellowknife Bay (Fig. 1), where extensive remote sensing, con-

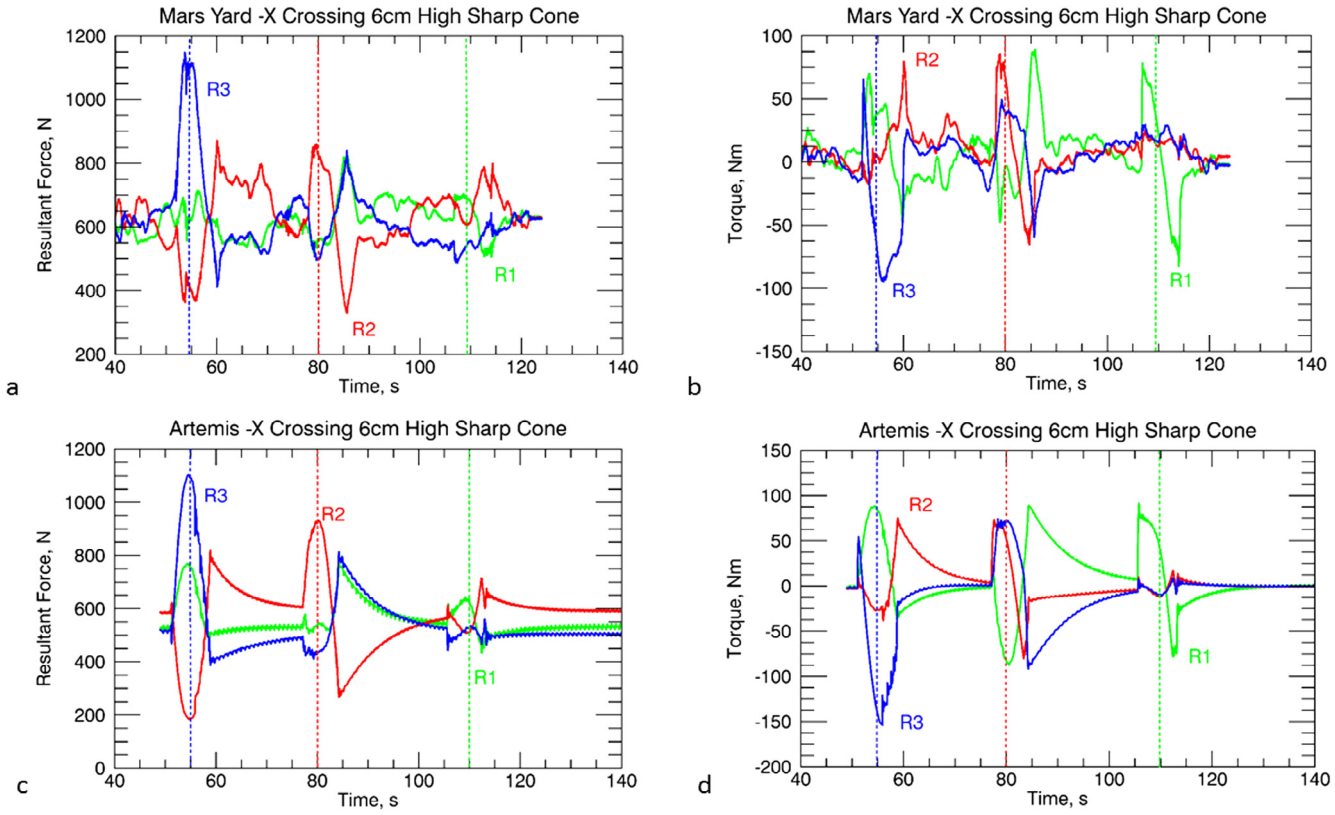

Fig. 6. **Resultant force as a function of time for Mars Yard and Artemis $-X$ drive.** (a) Resultant forces as function of time are shown for instrumented right side wheels on the Scarecrow rover driving in the $-X$ direction (backward drive) over the 6 cm high cone, simulating a sharp rock. (b) Plot of drive actuator torques for Scarecrow with positive torques for driving and negative torques for slowing down. (c) Resultant forces as function of time are shown for wheels for the Artemis model for Curiosity under Martian gravity driving over a 6 cm high cone. (d) Plot of drive actuator torques for the Artemis simulation with positive torques for driving and negative torques for slowing down. The trends in the plots are quite similar for Scarecrow and Artemis. Color-coded vertical dashed lines show cone crossings for the wheels. See text for detailed analysis of the forces and torques. (For interpretation of the references to colour in this figure legend, the reader is referred to the web version of this article.)

tact science, and drilling were accomplished on the Bradbury group, Sheepbed member, exposed as mudstone outcrops (Fig. 1). Just before traversing into Yellowknife Bay, Curiosity also made a series of measurements in a sand deposit trapped in a cluster of rocks, an area called Rocknest. MAHLI-based imaging of the rover showed that the wheels were in relatively pristine condition, even after ~500 m of traversing across the plains surfaces (Fig. 2).

After completing the measurement campaign on the mudstones exposed in Yellowknife Bay the rover was commanded to begin a long set of traverses to the southwest, continuing along dominantly the plains surfaces for a distance of ~4 km. Thermal inertias for the plains terrain averaged ~200 J m^{-2} K^{-1} $s^{0.5}$, consistent with regolith covered bedrock with some dispersed rocks (Arvidson et al., 2014) (Fig. 3a). Soon thereafter (~sol 440) the rover crossed from plains into terrain with slightly higher and more variable thermal inertia (~200–330 J m^{-2} K^{-1} $s^{0.5}$). This broad transition corresponded to increased areal exposures of well-indurated Bradbury group sandstone outcrops interpreted to have formed in fluvial-deltaic depositional environments. The sandstone exposures have been shaped by fracturing and wind erosion into outcrops with sharp, immobile surfaces (Fig. 3b). Images of the wheels acquired by MAHLI showed new punctures and cracks after a few of these outcrops were traversed (Fig. 4). Analysis of HiRISE images (McEwen et al., 2007) showed that the plains along the route to Mount Sharp transitioned to even more exposures of eroded and likely sharp sandstone outcrops, and then to broad plateaus capped by these sandstone deposits. Relatively planar and recessive mudstone bedrock was inferred to be exposed in the valleys located between the plateaus, variably covered by wind-blown sand ripples and regolith. This geomorphic pattern was interpreted to be a consequence of wind erosion, with more indurated sandstones capping the plateaus, and valleys formed by wind-induced scarp retreat, locally trapping wind-blown sands and regolith, and exposing underlying and less resistant mudstones.

The need to traverse the sharp sandstone outcrops led to an increased awareness of cumulative wheel damage, wheel lifetimes, and ways to minimize additional damage, including formation of a wheel anomaly investigation team to evaluate the mechanics of damage and wheel lifetime estimates, and a geomorphic mapping and analysis team to define rover paths that would minimize traverses across

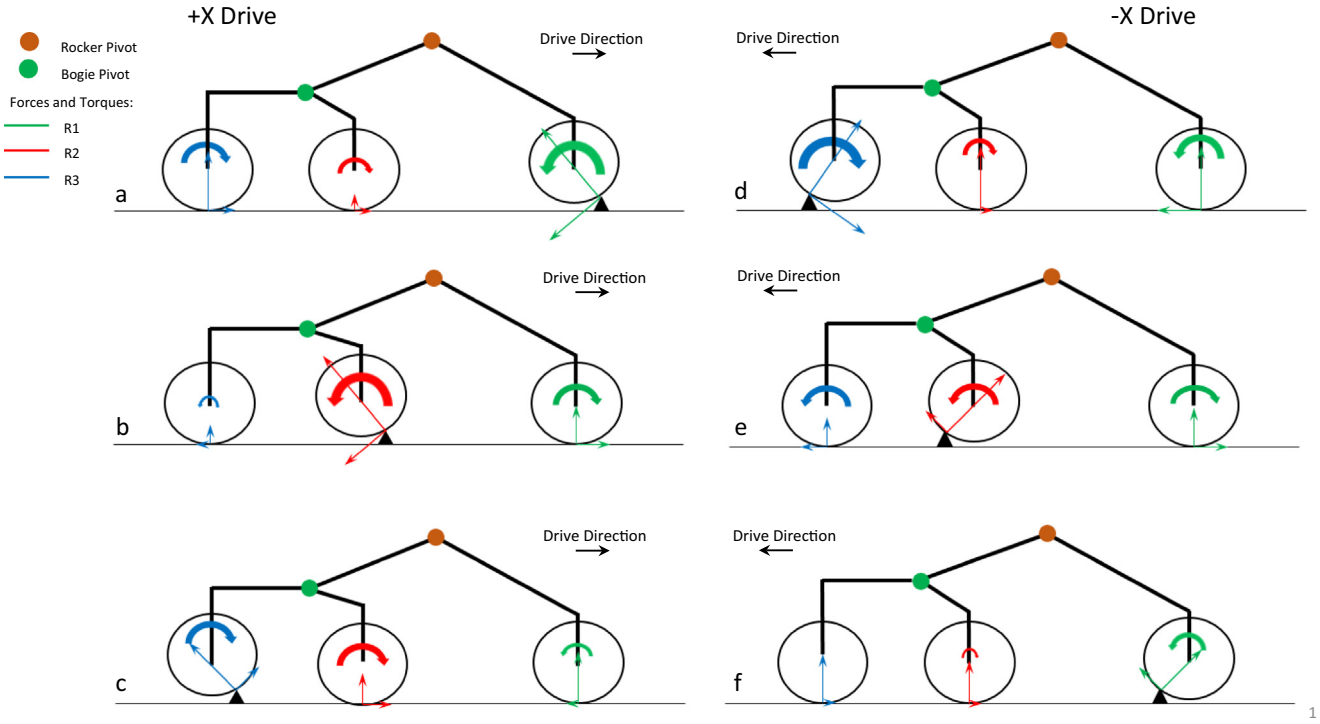

Fig. 7. **Suspension and wheel system free body diagrams.** Suspension and wheel system free body diagrams showing forces and torques for $+X$ and $-X$ drives describing the trends seen for Scarecrow and Artemis drives across the 6 cm high cone, simulating a sharp rock. Force and torque directions are shown, with relative force magnitudes represented by arrow lengths, and torque relative magnitudes represented by arrow thicknesses and lengths. Positive torques are shown with clockwise arrows for the $+X$ drive and counterclockwise arrows for the $-X$ drive. See text for detailed discussion.

sharp bedrock surfaces. The wheel anomaly investigations included a combined experimental and modeling effort to better understand the vehicle's suspension mechanics, and the relationship to punctures and crack initiation and propagation (Figs. 5–7). Geomorphic units were mapped and defined along strategic routes informed by the geologic setting of fluvial-deltaic-lacustrine strata and the likelihood of wheel damage (Figs. 8–18). These efforts led to best driving practices to avoid rock fields and outcrops with sharp rocks, informed by the geomorphic map units. A plan to drive through wind-blown sand ripple-filled valleys to cushion the wheel loads was contemplated, but rejected after the rover encountered very high slip values in the loose sands that dominated the ripple fields (Arvidson et al., 2016). An additional response to wheel damage was the periodic use of Curiosity's imaging systems to inventory punctures and cracks, primarily taking advantage of MAHLI to see all six wheels, using intervening drive motions between imaging observations.

In the next sections of this paper results are summarized for the experiments and modeling of rover suspension mechanics and the relationship to wheel punctures and crack development, geomorphic mapping and path planning to minimize wheel damage, cumulative wheel damage, and implications for wheel lifetimes given the terrain to be encountered as the rover ascends Mount Sharp.

4. Mechanics of wheel damage

To further understand the suspension mechanics and the relationship to wheel punctures and crack propagation, the wheel anomaly investigation team initiated a suite of experiments using the Scarecrow rover, an engineering version of Curiosity, in the Mars Yard testbed at the Jet Propulsion Laboratory. Scarecrow has 3/8 of the flight rover's mass and is instrumented with axle-mounted 6 degree of freedom force/torque sensors to re-create and measure wheel loading under Mars gravitational conditions (Heverly et al., 2013). The wheel anomaly investigation team also initiated a suite of simulations using Artemis, a computationally fast, semi-empirical terramechanics software tool that models the Curiosity rover under Mars gravity for tactical path planning and first-order estimation of terrain properties (Zhou et al., 2014; Arvidson et al., 2014, 2016). Additional activities included theoretical modeling of puncture and crack initiation and propagation dynamics, although these will not be covered in this paper as the Mars Yard tests and Artemis simulations provide the information needed to understand suspension mechanics and how the chosen mode of drive actuation initiates and extends puncturing and cracking.

The static wheel loading for Curiosity under Martian gravity on flat, level terrain is approximately the same for the left and right wheels, with values of 564 N, 636 N, and 458 N for wheels 1–3. The static wheel loads would

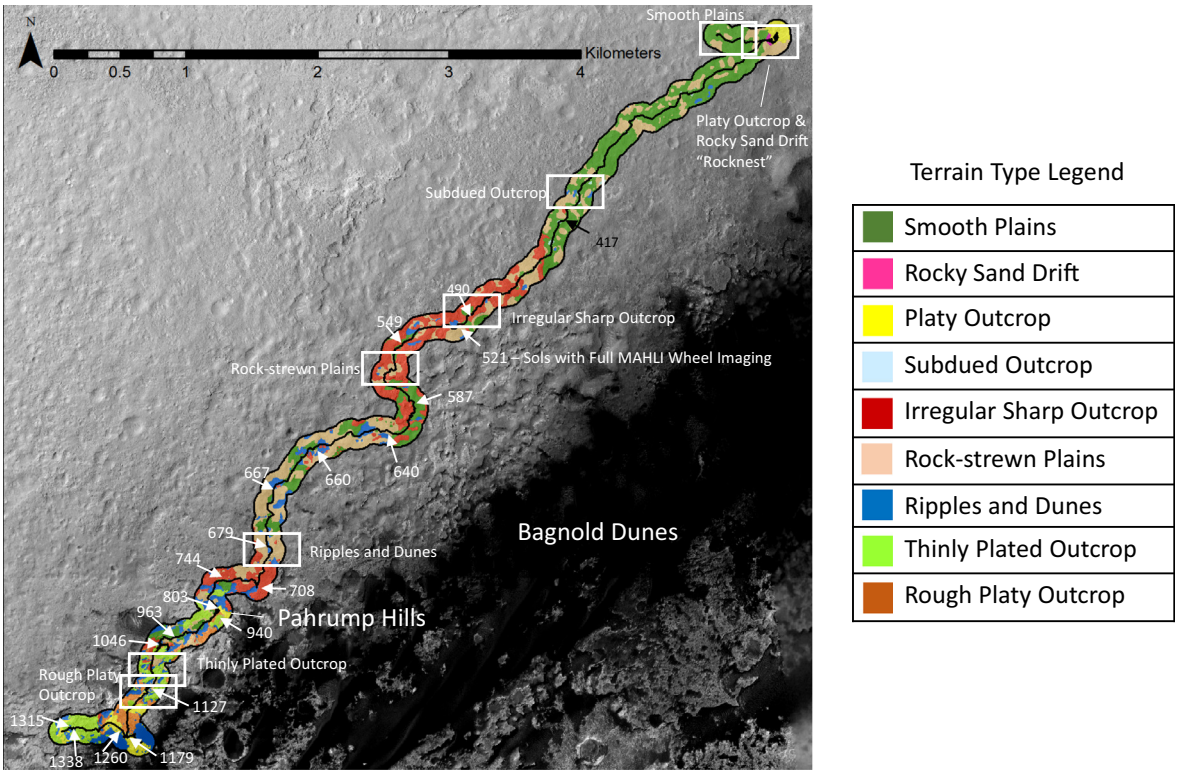

Fig. 8. **Geomorphic map along Curiosity traverse.** Geomorphic map focused along traverses with locations and sols shown for MAHLI wheel imaging stops. Map units and terrain descriptions provided in Table 1. Type localities for each unit are shown as labeled white boxes, with Navcam mosaics for each unit provided in Figs. 9–17. The mapping is based on a 100 m corridor on either side of Curiosity's traverses from Bradbury Landing to the Naukluft Plateau. Sols are shown on the map and correspond to locations where MAHLI full wheel imaging was done to inventory wheel damages. The Pahrump Hills location is shown and corresponds to a rapid increase in the left wheel 1 damage rate as discussed in the text. HiRISE mosaic is used as the base for the map.

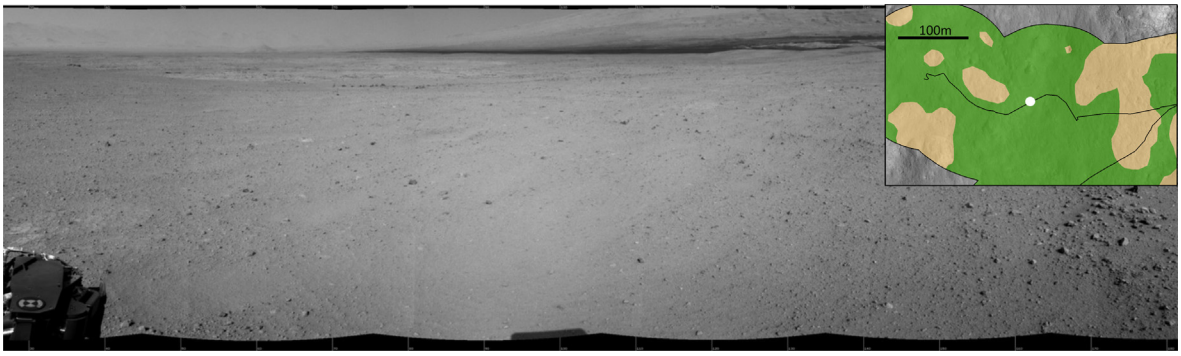

Fig. 9. ***Smooth plains*: Sol 40 Navcam mosaic.** Navcam mosaic centered on the white dot is shown for the *smooth plains* map unit type locality: rolling or hummocky plains dominantly covered with regolith with few dispersed rocks. Also shown on this and subsequent unit type locality figures is a map inset keyed to Fig. 8 and Navcam mosaics used are given in Table 2. The mosaic extends from ~30° to 175° in azimuth clockwise from north.

of course increase on sloped terrain for the downhill wheels or decrease for the uphill wheels. Laboratory and Mars Yard tests with immobile terrestrial rocks shaped to sharp surfaces by wind (i.e., ventifacts) showed that static loads alone can initiate microcracks, but are unlikely to cause punctures, even at the tilts experienced by Curiosity during its drives across the sharp sandstone outcrops. Punctures on 0.75 mm aluminum were found by experiment to occur at ~800 N for sharp metallic cones with a tip radius of ~0.03 cm or less. Tests with wind-shaped rocks collected from the Mojave Desert imply larger loads would be needed, perhaps >1500 N for punctures to occur, although these tests were conducted on a limited number of samples. For purposes of this paper punctures are assumed to be generated for the sharpest rocks if contact forces are larger than ~800–1000 N.

To better understand the suspension mechanics and the relationship to wheel punctures and cracks Scarecrow was

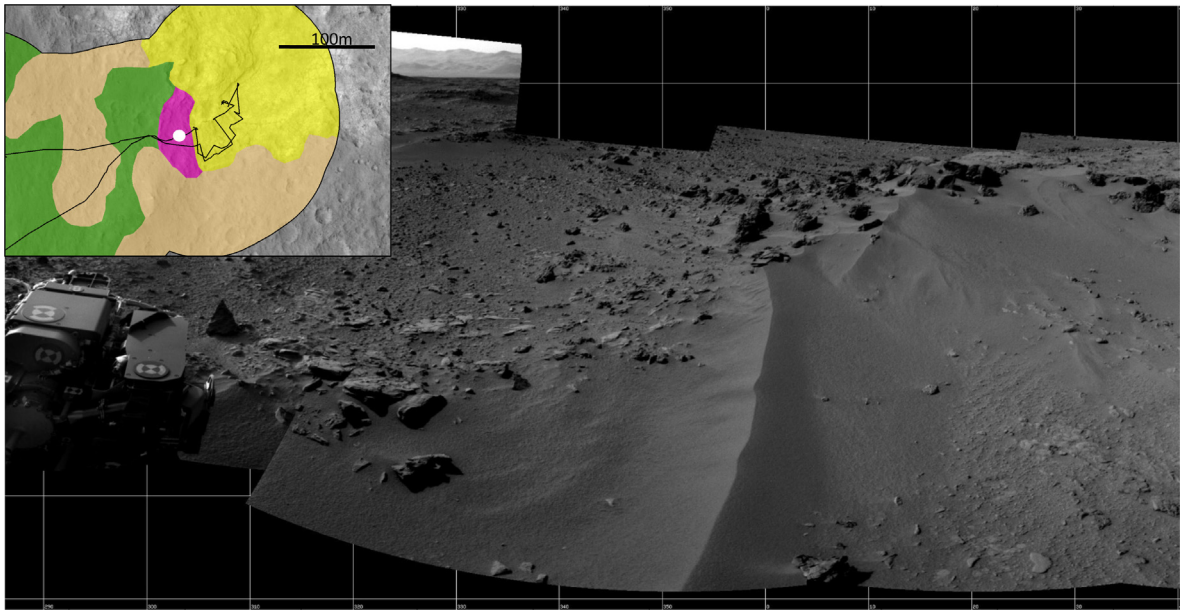

Fig. 10. ***Rocky sand drift*: Sol 55 Navcam mosaic.** Navcam mosaic is shown for the *rocky sand drift* map unit type locality: rock fields that trapped wind-blown sand deposits, e.g. "Rocknest". The mosaic extends from ~285° to 40° in azimuth clockwise from north.

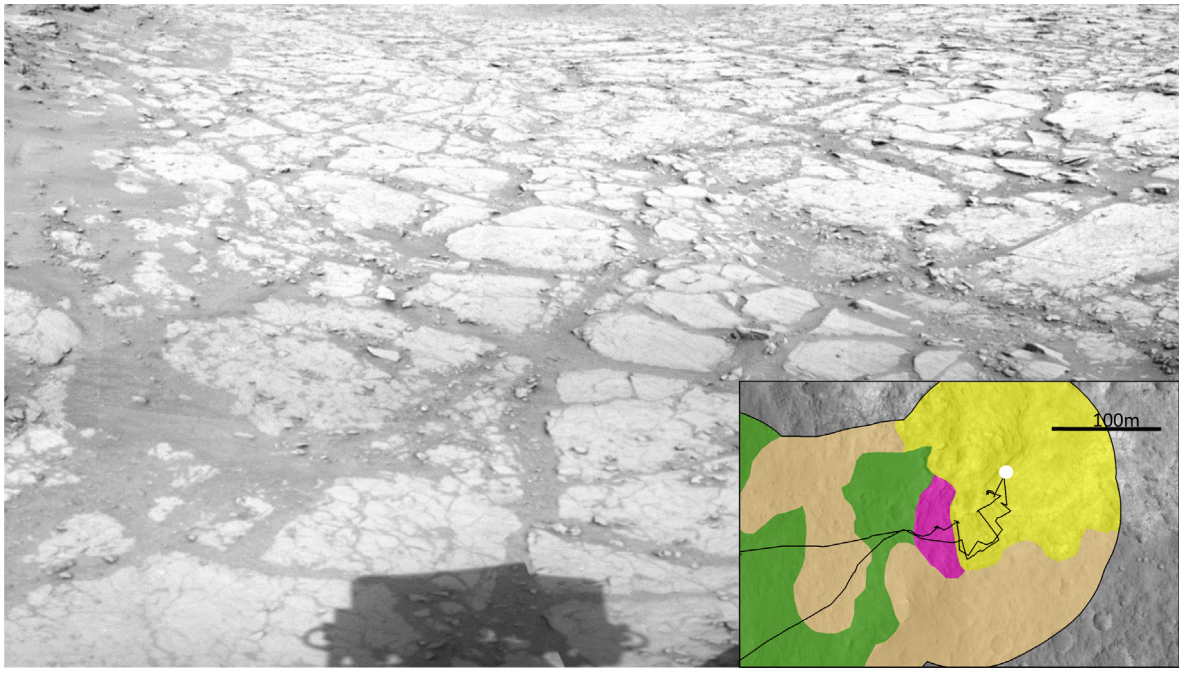

Fig. 11. ***Platy outcrop*: Sol 130 Navcam mosaic.** Navcam mosaic is shown for the *platy outcrop* map unit type locality: bedrock exposed as relatively planar polygons with few sharp edges or dispersed rocks, largely mudstones. The mosaic extends from ~30° to 120° in azimuth clockwise from north.

driven both forward (in the $+X$ direction, L1 and R1 wheels leading) and backward (in the $-X$ direction, L3 and R3 wheels leading), with the right wheels crossing over an immobile 6 cm high right-circular steel cone with 60° included angle and a 0.13 cm radius contact point. The large tip radius of curvature was chosen to minimize likely puncturing and cracking so that the experiments could be conducted a number of times with intact wheel surfaces. The cone was immobile and embedded within cohesive, poorly sorted regolith on a flat, horizontal surface. Resultant contact forces and drive actuator torques measured in the Mars Yard for each right wheel in contact with the ground and the cone are given in Figs. 5a-b and 6a-b, respectively, for $+X$ and $-X$ drives. Corresponding values for Artemis simulations over a cone with similar geometry are provided in Figs. 5c-d and 6c-d, using the ADAMS standard contact model between the wheels and surface (Zhou et al., 2014). The force and torque patterns for the

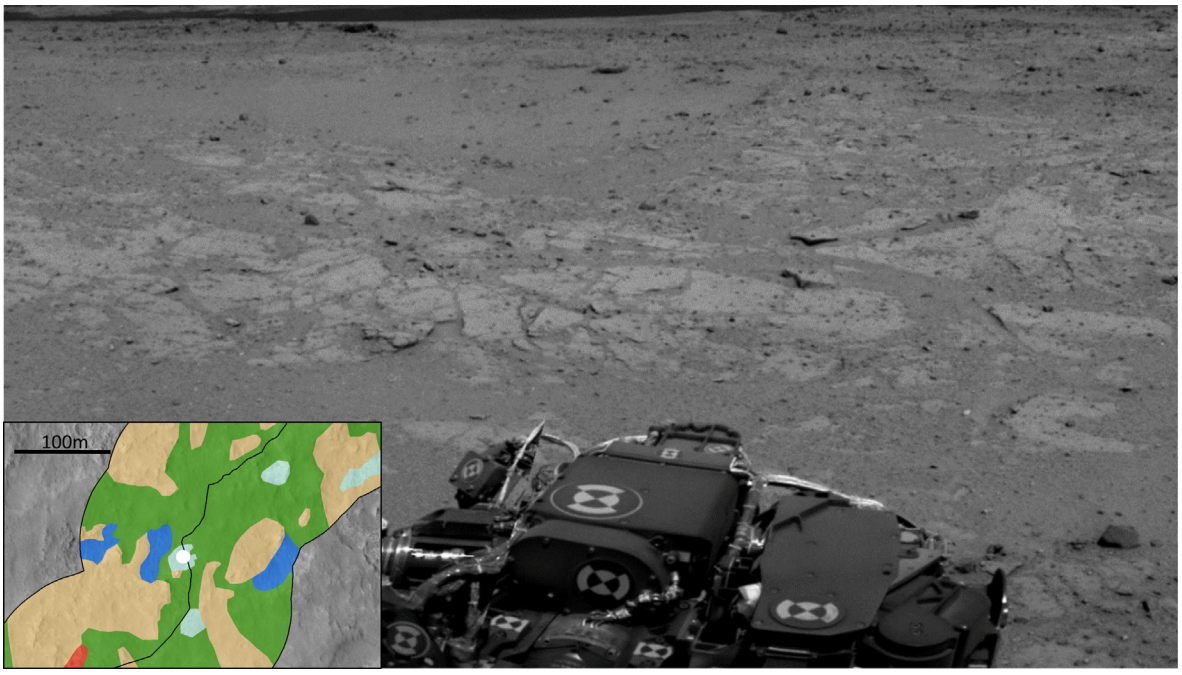

Fig. 12. ***Subdued outcrop*: Sol 408 Navcam mosaic.** Navcam mosaic is shown for the *subdued outcrop* map unit type locality: patches of partially disaggregated conglomerate outcrop, not sharp, found predominately in the first 500 sols. The mosaic extends from ~100° to 165° in azimuth clockwise from north.

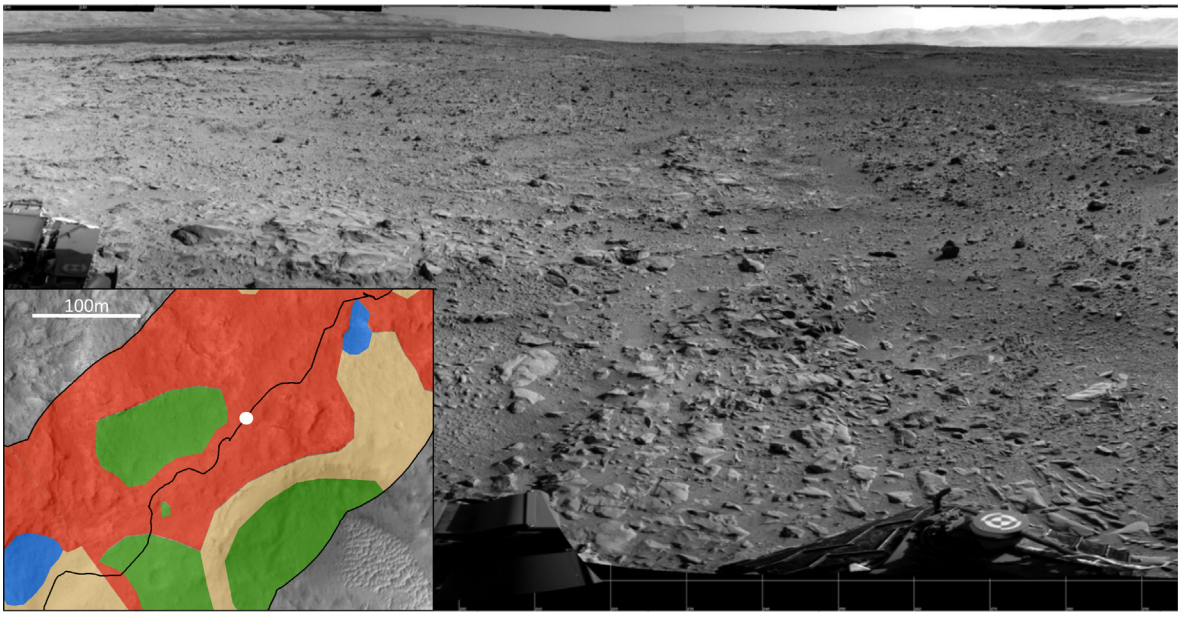

Fig. 13. ***Irregular sharp outcrop*: Sol 470 Navcam mosaic.** Navcam mosaic is shown for the *irregular sharp outcrop* map unit type locality: rough outcrop with varying strewn rock fields; fluvial and deltaic sandstones that have been differentially eroded to expose sharp rock surfaces. The mosaic extends from ~135° to 280° in azimuth clockwise from north.

experiments and simulations are quite similar. This implies that Artemis results can be used to help explain the mechanics of the traverses over the obstacles, including the generation of forces capable of puncturing the 0.75 mm thick aluminum wheel skin. Resultant wheel-to-obstacle reaction force components (wheels to surfaces) and drive actuator-induced torque (hereafter referred to as "torque") diagrams are provided in Fig. 7a-f for the $+X$ and $-X$ drives.

The following paragraphs describe the behavior of each of Scarecrow's right-side wheels during both $+X$ and $-X$ drive operations while negotiating the 6 cm tall cone. The difference in the behavior of each wheel is largely related to the location of the wheel with respect to its adjoining

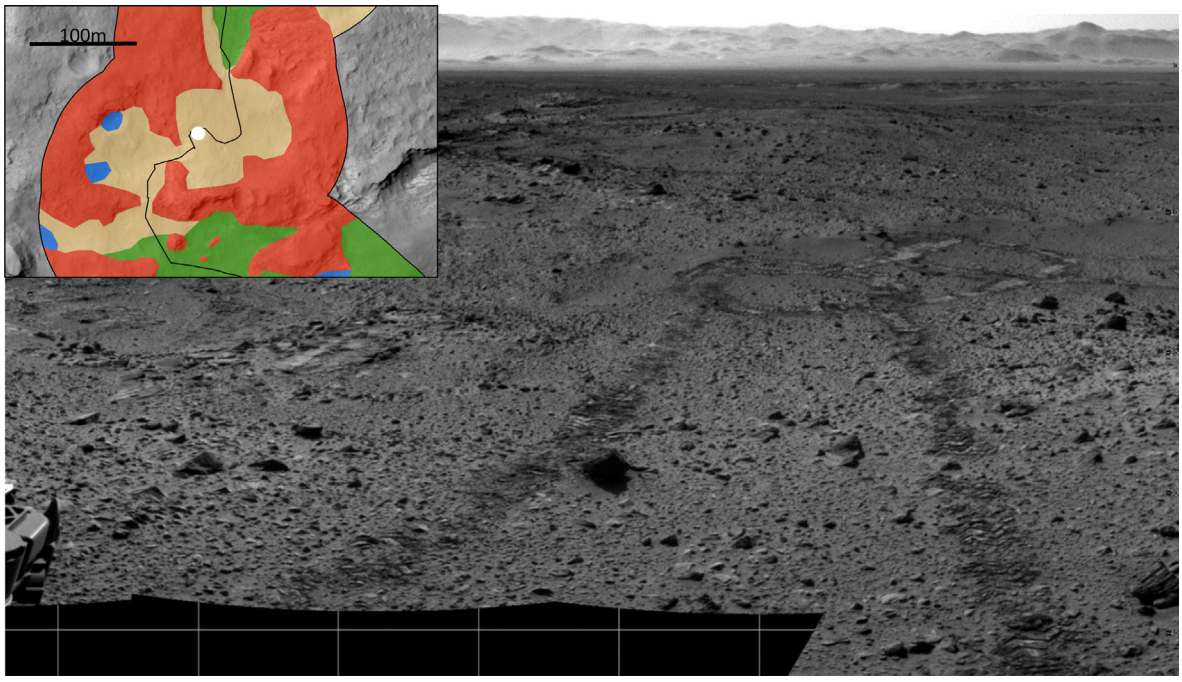

Fig. 14. ***Rock-strewn plains*: Sol 563 Navcam mosaic.** Navcam mosaic is shown for the *rock-strewn plains* map unit type locality: rolling or hummocky plains dominantly covered with regolith but with abundant strewn rock fields. The mosaic extends from ~265° to 350° in azimuth clockwise from north.

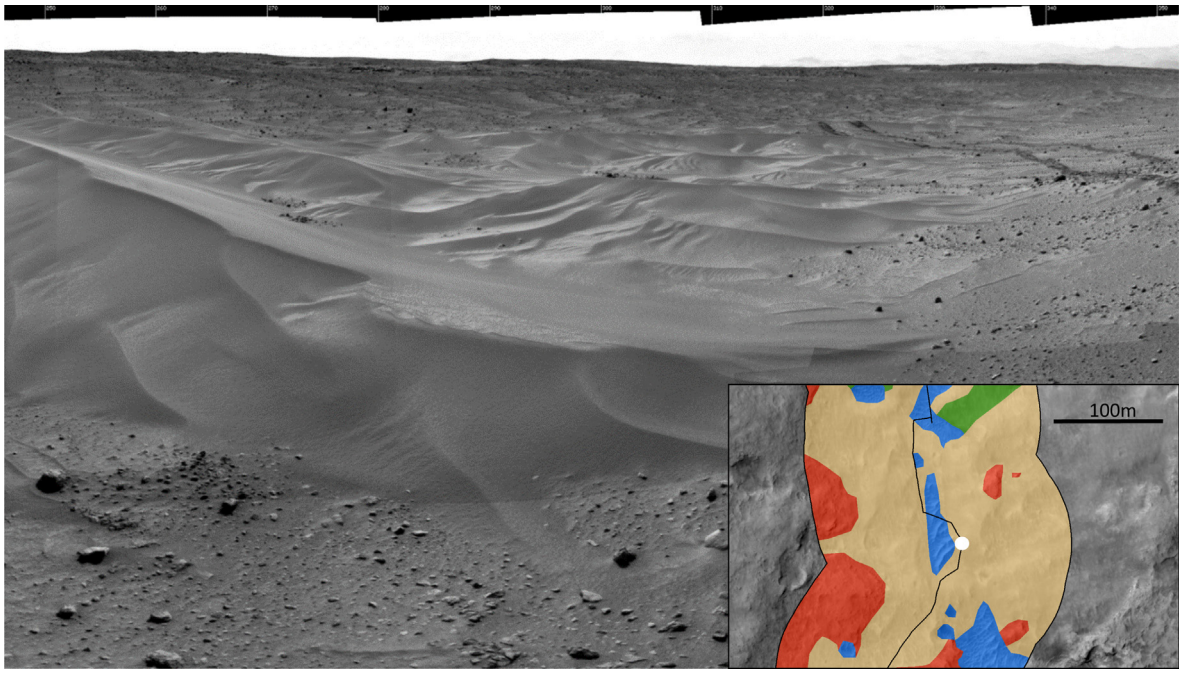

Fig. 15. ***Ripples and dunes*: Sol 683 Navcam mosaic.** Navcam mosaic is shown for the *ripples and dunes* map unit type locality: meter-wavelength ripples to large sand dunes, wide variation in sizes, largely accumulated in topographically low areas. The mosaic extends from ~240° to 350° in azimuth clockwise from north.

suspension rocker or bogie pivot, together with the vehicle drive direction. For example, in Fig. 7a R1 encounters the obstacle while leading the rocker pivot, and is thus operating on a leading suspension arm. The converse is detailed in Fig. 7f, when R1 encounters the obstacle while behind the rocker pivot, thus operating on a trailing suspension arm. For this discussion positive drive torque indicates torque acting to provide thrust in the intended direction of vehicle motion. In Fig. 7 clockwise torques are positive for the $+X$ drive and counterclockwise for the $-X$ drive.

For the $+X$ drive when the leading wheel (R1) initially encounters the cone (Fig. 5a-d) positive torque is applied

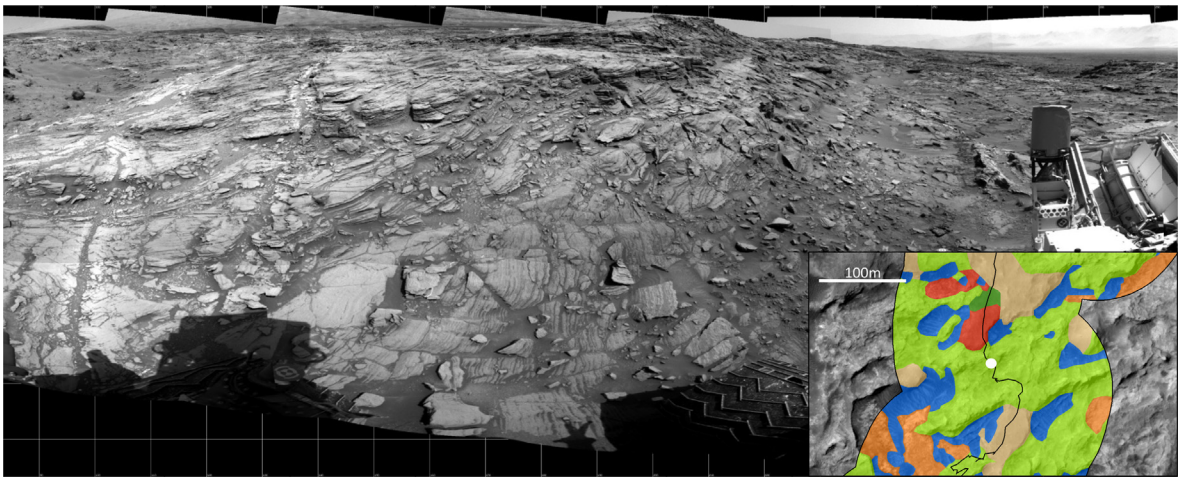

Fig. 16. ***Thinly plated outcrop*: Sol 1093 Navcam mosaic.** Navcam mosaic is shown for the *thinly plated outcrop* map unit type locality: thinly laminated outcrops, largely aeolian sandstones (Stimson formation) that unconformably overlie fluvial-deltaic-lacustrine deposits. The mosaic extends from ~90° to 290° in azimuth clockwise from north.

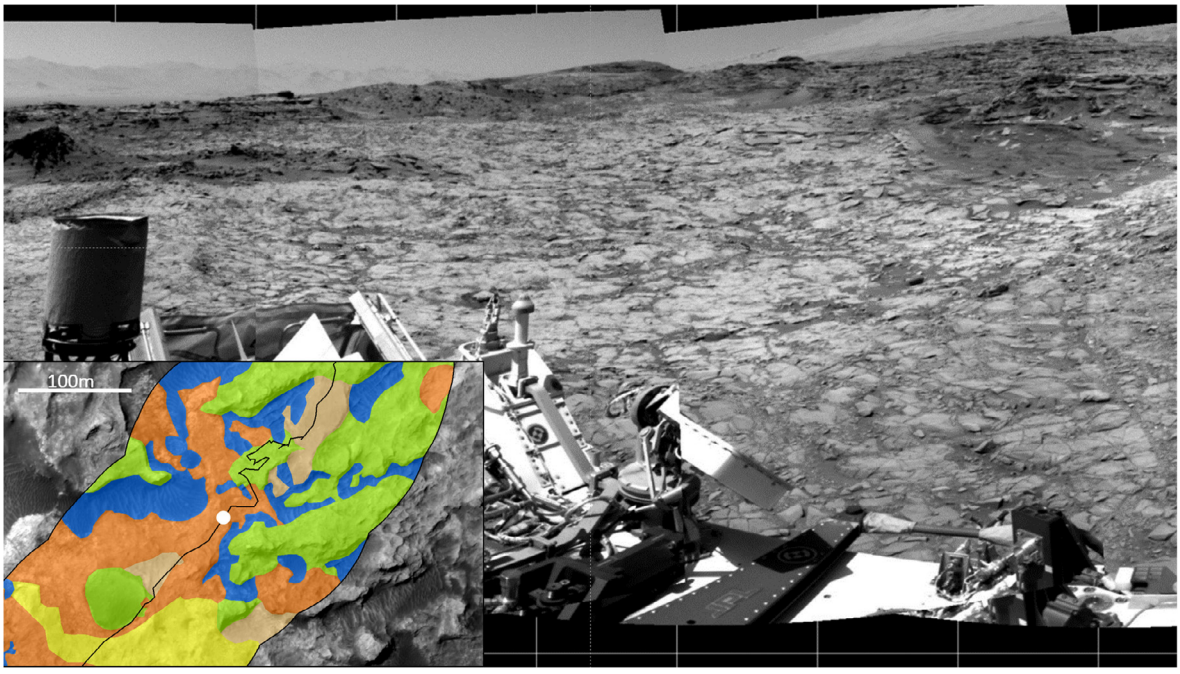

Fig. 17. ***Rough platy outcrop*: Sol 1153 Navcam mosaic.** Navcam mosaic is shown for the *rough platy outcrop* map unit type locality: bedrock exposed as relatively planar polygons, some sharp edges and dispersed rocks, largely mudstones. The mosaic extends from ~35° to 115° in azimuth clockwise from north.

to begin lifting the wheel over the obstacle. R1 must take a longer path length over the cone as compared to the other wheels. This results in torque values quickly falling and changing direction to negative torque values after initial obstacle engagement. The change to negative torque values is a consequence of R1 trying to maintain its commanded angular velocity. At the same time the other wheels push R1 onto the obstacle as they maintain their commanded angular velocities. A force couple about the rocker pivot (Fig. 7a) also acts to transfer additional load to R1. The resultant force value resists the vehicle's motion and R1 develops loads against the obstacle that are much higher than the static normal load, and likely to cause puncturing and tearing. The R3 behavior while R1 engages the obstacle shows the converse phenomenon of a wheel operating on a trailing arm while providing drive thrust. In this case the trailing R1 force couple acts to push that wheel into the ground, enabling it to supply the dominant drive torque and consequent thrust. The resulting R3 force creates a moment about the bogie pivot which is balanced by the substantial unloading of R2, forcing R1 and R3 to support a larger percentage of the vehicle weight. On high friction

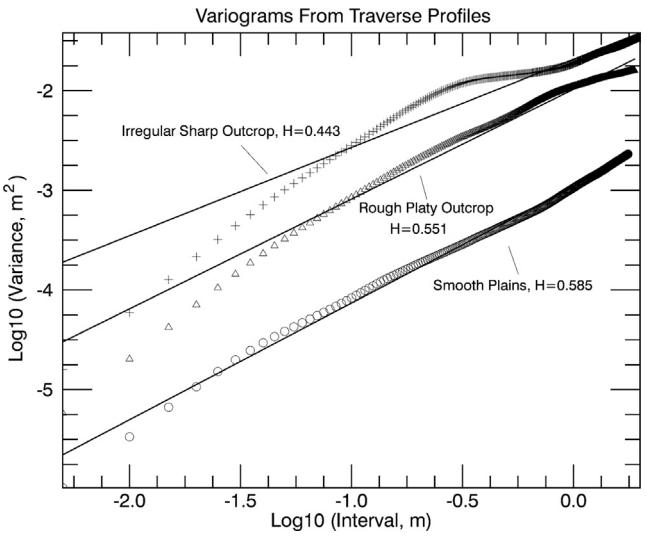

Fig. 18. **Variograms for *smooth plains, rough platy outcrop, and irregular sharp outcrop* geomorphic units.** Hurst exponents are fit using least squares methods and correspond to the slope of the log-log linear fits. The Hurst exponent is equal 2-D, where D is the fractal value for a topographic profile. The *irregular sharp outcrop* is the roughest surface at all length scales and exhibits a clear multi-fractal topographic profile. Data derived from elevation maps generated from Curiosity imaging data summarized in Table 3 and selected to be along traverses for 20 m distance closest to the end of drive location for representative terrain units.

terrains Scarecrow driving in the $+X$ direction frequently exhibited a R2 'wheelie' as R1 engaged an obstacle and R3 provided substantial thrust. This is exacerbated in $+X$ driving cases because R2 lacks a steering actuator and thus has less non-suspended mass to generate a resistive torque. R2 also acts on a smaller moment arm than R3, again resulting in less resistive torque. Once R1 has finished negotiating the cone (Fig. 5a-d), all three wheels encounter the surface surrounding the obstacle as the vehicle settles, with the corresponding wheel force and torque peak and decay trends moving toward values typically found on flat, horizontal terrain.

As R2 engages the obstacle during a $+X$ drive operating on a leading arm (Fig. 5a-d), this wheel's torque briefly climbs to positive values to lift it onto the obstacle. Similar to the R1 $+X$ case, the increased path length over the obstacle for R2 is not compensated for by the remaining drive actuators, which do not change their Ackerman arc commanded angular velocities as R2 encounters the obstacle. The R2 torque thus quickly falls and changes sign as that wheel is pushed into the obstacle by the thrust of other wheels. The resulting force couple about the bogie pivot (Fig. 7b) acts to transfer additional weight from R3 to R2 (Fig. 5a and c), with the direction of the resultant force resisting the vehicle's motion. This causes R2 loads against the obstacle that are much higher than the static normal load and likely to cause damage. R1 provides the dominant positive torque during this encounter (Fig. 5b and d). As R2 egresses the obstacle (Fig. 5a-d), force and torque peak and decay signatures return to values that are typical for drives on flat, horizontal surfaces as the vehicle resettles. The reduction in R2 force, and subsequent increases in R1 and R3 forces, correspond to the increase in R3 positive torque values. These persist until R3 settles the inter-mobility system forces. During Scarecrow testing on high friction terrains R2 tended to hover or 'wheelie' as it egressed an obstacle because R3 was unable to slide in the $-X$ direction and settle the suspension. The cyclic unloading and often violent re-contact of R2, after a R2 'wheelie,' would increase the probability of damage. R3 positive torque and resultant thrust values also contribute to having R2 hover above the surface during obstacle egress.

As R3 engages the cone during a $+X$ drive it is operating on a trailing arm (Fig. 5a-d). The R3 torque climbs, and unlike the leading arm R1 case, remains at positive values for the duration of the engagement with the obstacle. The increased required path length for R3 is not compensated for by the other wheel drive actuators, although for a trailing arm situation the direction of the resultant force acts to assist the vehicle's motion by lifting R3 over the obstacle. The positive R3 drive torque produces a force couple about the bogie pivot (Fig. 7c) and does not cause a transfer of an additional load from R2 to R3 (Fig. 5a and c). These loads do not climb far enough beyond the static load to initiate single event punctures or likely even accelerate low-cycle fatigue. This is the primary reason why driving in the $+X$ direction is predicted to cause only minimal R3 damage. The R2 torque sustains positive values while R3 negotiates the obstacle, in part because R2 slides in the $-X$ direction as R3 is lifted. The combination of thrust produced by both R2 and R3 while R3 engages the obstacle also results in a negative R1 actuator torque. This is indicative of other R2 and R3 thrust values that should lead to increased angular velocity of R1. However, R1 actuator maintains its commanded velocity during this situation. As R3 egresses the obstacle R2 slides in the $+X$ direction to settle the suspension. This produces negative R2 torques and creates a couple about the bogie pivot that acts to decrease the R3 load as the suspension settles.

R3 is the leading wheel for the $-X$ drive (Fig. 7d-f). As R3 engages the obstacle during a $-X$ drive it is operating on a leading arm (Fig. 6a-d). The R3 torque briefly climbs to positive values to lift it onto the obstacle. Similar to other leading arm cases, the increased required path length is not compensated for by the remaining drive actuators. Thus, the R3 torque quickly falls and changes sign as the wheel is pushed onto the obstacle by the R1 trailing arm. The R1 thrust is evidenced by this wheel's sustained positive torque values (Fig. 6b and d). The resulting force couple about the bogie pivot (Fig. 7d) acts to transfer significant load from R2 to R3 (Fig. 6a and c), with the direction of the resultant force resisting the vehicle's motion and acting to push R3 onto the obstacle. Resultant loads are much higher than the static normal load and likely to cause damage. In fact, during $-X$ direction test cases with the Scarecrow R3 was found qualitatively to

undergo the highest degree of damage. As R3 egresses the obstacle (Fig. 6a-d), R2 slides against the vehicle's direction of travel, creating positive R2 torque values as the suspension settles. Positive R2 torques during $-X$ drives create a couple about the bogie pivot that acts to decrease the R3 load during settling.

As R2 engages the obstacle during a $-X$ drive, it operates on a trailing arm (Fig. 6a-d), and responds similarly to the $+X$ trailing arm case in which the R3 torque remains at positive values for the duration of obstacle engagement. The direction of the resultant force acts to assist the vehicle's motion by lifting R2 over the obstacle. The positive R2 torque creates a force couple about the bogie pivot (Fig. 7e) that acts to transfer additional weight from R3 to R2 (Fig. 6a and c), thereby increasing loads to high enough values to perhaps cause wheel damage. R3 torque sustains positive values while R2 negotiates the obstacle, in part because R3 slides in the $+X$ direction as R2 is lifted while driving in the $-X$ direction. The combination of thrust produced by R2 and R3 while R2 engages the obstacle also creates negative R1 torques. This creates a couple about the rocker pivot that acts to decrease R1 load. As R2 egresses the obstacle R3 slides in the direction of travel to settle the suspension. This produces negative R3 torques and creates a couple about the bogie pivot that acts to decrease the R2 load as the suspension settles.

R1 produces the best load distribution as it engages the obstacle during a $-X$ drive because it operates on the longest trailing arm of any configuration (Fig. 6a-d). The R1 torque values remain positive for the duration of obstacle engagement. The direction of the resultant force acts to assist the vehicle's motion by lifting R1 over the obstacle. The R1 trailing arm is sufficiently long that the force couple created about the rocker pivot (Fig. 7f) as a result of the positive R1 drive torque does not transfer appreciable load among wheels (Fig. 6a and c). In addition it does not generate much wheel sliding. As R1 egresses the obstacle the additional path length does become evident as that wheel slides in the direction of travel, thereby creating negative torque values. The resulting couple created about the rocker pivot during egress acts to increase bogie loading, which is evidenced by the slight increase, and subsequent decay, in R2 and R3 forces as the suspension settles.

Results from the Mars Yard experiments and Artemis simulations show that resultant forces as high as twice the static loads on level terrain, combined with significant negative torques, are likely when encountering sharp rocks for wheels operating on leading arms; i.e. wheels 1 and 2 when driving in the $+X$ direction, and wheel 3, and to a lesser extent wheel 2 when driving in the $-X$ direction. Details would of course change depending on obstacle heights and shapes, whether or not the traverses are on tilted or level surfaces, and the nature of wheel-surface frictional contacts with terrain surrounding the obstacle. Even so it is clear that wheel punctures and crack propagation are likely a combination of wheel loading conditions, the mechanics of the rocker-bogie based suspension system, and the constant angular velocity commanded of the drive actuators while traversing sharp, embedded obstacles. Further, additional Mars Yard tests show that existing wheel puncture and low cycle fatigue crack damage propagates more easily with less force as damaged zones are enlarged when encountering rocks and/or having the rover turn in place over rocks.

5. Geomorphic mapping

Given the damage to the wheels observed during initial traverses across sandstone outcrops shaped by fracturing and wind into immobile sharp surfaces it became important to avoid these surfaces and to bias drives to cross less egregious terrains. This led to a systematic mapping effort along the preferred traverse corridor to Mount Sharp, identifying geomorphic terrain units informed by the geologic setting, with a focus on units that directly relate to likely wheel damage rates as a function of traverse distance (Figs. 8–17, Table 1).

Detailed assessment of orbital and Curiosity observations indicate that the Bradbury group Sheepbed member and Murray formation mudstones formed in a lacustrine environment, with Bradbury group fluvial and deltaic sandstones (with some conglomerates) accumulating over the mudstones as the fluvial and deltaic deposits extended to the south (Fig. 1) (Grotzinger et al., 2015). Specifically, Bradbury group fluvial-deltaic-lacustrine deposits interfinger with and transition to the Murray formation mudstones. After a period of erosion the fluvial-deltaic-lacustrine deposits were unconformably overlain by wind-blown sandstones called the Stimson formation (Banham et al., 2016). The fluvial-deltaic-lacustrine deposits underlie the plains that Curiosity encountered during its first ~5 km of traverses, including exposed Sheepbed member mudstone strata in Yellowknife Bay as part of the Bradbury group (Fig. 1). As Curiosity traversed the plains to the southwest sandstone outcrops were encountered, followed by more dissected terrains with sandstones capping plateaus and mesas. Valleys floored by the less resistant Murray formation mudstones, variably covered by modern wind-blown ripple deposits and regolith. By the time the rover reached the Naukluft Plateau the Stimson formation wind-blown sandstones that uncomfortably overlie the Murray formation mudstones were being traversed.

The strata encountered and their erosional styles were used to create a systematic geomorphic map within a 100 m distance on either side of Curiosity's traverses, starting at ~4.2 km traverse distance (~sol 440), when it became apparent that wheel damages were occurring at a high rate during drives over sharp sandstone outcrops. Predictive maps were generated using HiRISE images and updated based on observations from Curiosity's imaging systems. The whole traverse path was remapped for this paper using orbital and Curiosity data, along with defining type localities for each of the newly mapped nine mapped units (Figs. 8–17). These units are described in the chrono-

Table 1
Geomorphic terrain units.

Geomorphic unit	Description	Mobility issues
Smooth Plains	Rolling or hummocky plains dominantly covered with regolith with few dispersed rock underlain by Bradbury group fluvial-deltaic-lacustrine strata	Relatively innocuous traverses with pebbles and cobbles rotated or pushed into regolith when encountering wheels
Rocky Sand Drift	Rock fields that trapped modern wind-blown sand deposits, e.g., Rocknest	Rare occurrences easily avoided
Platy Outcrop	Bedrock exposed as relatively planar polygons with few sharp edges or dispersed rocks. Bradbury group Sheepbed member and Murray formation mudstones formed in a lacustrine environment	Relatively innocuous traverses on flat-lying plates with low areal density of dispersed rocks
Subdued Outcrop	Bedrock exposed slightly above surrounding regolith-covered plains and dominated by fluvial-deltaic conglomerates with some sandstones of the Bradbury group	Avoided during traverse planning
Irregular Sharp Outcrop	Topographically rough outcrops with varying strewn rock fields composed of well-cemented Bradbury group fluvial sandstones that have been differentially eroded to expose sharp rock surfaces	Most egregious terrain to traverse with irregular, sharp outcrops that likely produced highest rate of wheel tears
Rock-strewn Plains	Rolling or hummocky plains dominantly covered with regolith with abundant strewn rock fields deposited as impact ejecta or by differential erosion of relatively indurated deposits, likely sandstones	Traversing over larger rocks either rotated them or lifted the wheels, likely causing some damage
Ripples and Dunes	Meter-wavelength modern ripples to large sand dunes, wide variation in sizes, largely accumulated in topographically low areas	Single ripples traversed without difficulty. Ripple fields and dunes avoided because of high probability of embedding
Thinly Plated Outcrop	Wind-blown, cross-bedded sandstones of the Stimson formation. Forms capping unit with thin, platy weathering style without many sharp rock surfaces	Relatively friable outcrop and lack of sharp edges not a major issue for wheel damage
Rough Platy Outcrop	Bedrock exposed as relatively planar polygons eroded to more irregular surfaces as compared to platy outcrop unit. Some resistant vein materials standing above rest of outcrop. Murray formation mudstones formed in a lacustrine environment	Intermediate in wheel damage as compared to *platy outcrop* and *irregular sharp outcrop*

logical order in which good exposures and thus type localities were encountered during Curiosity's traverses.

The *smooth plains* unit dominated exposures from Bradbury Landing to Yellowknife Bay (Fig. 9), and exiting Yellowknife Bay until extensive patches of irregular, sharp sandstone outcrops of the Bradbury group were encountered. These rolling and largely regolith-covered plains presented innocuous drives in which relatively small pebbles and cobbles were pushed into the regolith by the wheels, or larger cobbles were rotated by the wheels, both without discernable wheel damage.

Wind-blown sand trapped by a cluster of boulders was encountered just before entering Yellowknife Bay and this unit is called *rocky sand drift*, with a type locality at Rocknest, where initial scooping and analytical measurements were accomplished (Fig. 10). Rocky sand drifts were easily avoided while traversing the plains.

Yellowknife Bay exposed platy, flat-lying Sheepbed mudstones of the Bradbury group, with few strewn rocks and occasional uplifted plates. This unit is named *platy outcrop* unit (Fig. 11). The *platy outcrop* unit was encountered in many other localities along traverses (Fig. 8), particularly in valleys, and corresponds to Murray formation mudstones (Fig. 1).

The *subdued outcrop* unit encountered during the plains traverses represents loosely consolidated conglomerates of the Bradbury group (Williams et al., 2013), sporadically exposed, together with some sandstones, and were avoided by careful path planning (Fig. 12).

As noted the extensive outcrops of Bradbury group sharp sandstones were encountered on the plains, just before the more dissected plateau and valley system. The type locality for the *irregular sharp outcrop* is shown in Fig. 13.

The plains traversed after leaving Yellowknife Bay occasionally exhibited a relatively high abundance of dispersed rocks and is mapped as *rock-strewn plains* (Fig. 14). These rock fields are interpreted to be what is left after significant erosion of resistant sandstones. Some may be related to ejecta deposits.

Wind-blown ripples of loose sands were encountered in valleys traversed to avoid the sandstone outcrops. Extensive ripple fields were found to cause Curiosity to undergo unacceptably high values of slip when all wheels were in sand. Thus extensive ripple fields were avoided during subsequent traverses (Arvidson et al., 2016). This unit is called *ripples and dunes* (Fig. 15). For simplicity this unit also includes the Bagnold dunes, which were also avoided because of likely mobility problems.

Wind-eroded exposures of the Stimson formation are finely cross bedded sandstones that cap the other bedrock units and erode to form outcrops that are topographically rough and occupy plateaus and mesas (*thinly plated outcrops*, Fig. 16). These deposits became common as Curiosity approached the Naukluft Plateau. At the wheel scale the outcrops have been eroded to thin, platy, weakly indurated rocks that lack sharp edges and were typically crushed by the rover's wheels.

Table 2
Navcam mosaics used to illustrate geomorphic unit characteristics.

Type locality	Sol	Product ID
Smooth Plains	40	N_L000_0040_EDR004CYLTS_0916_DRIVEM1
Rocky Sand Drift	55	N_L000_0055_EDR004CYLTSB3416_DRIVEM1
Platy Outcrop	130	N_L000_0130_EDR005CYLTS_1662_DRIVEM1
Subdued Outcrop	408	N_L000_0408_EDR017CYLTS_0000_DRIVEM1
Irregular Sharp Bedrock	470	N_L000_0470_EDR024CYLTSB0000_DRIVEM1
Rock-Strewn Plains	563	N_L000_0563_EDR029CYLTSB0000_DRIVEM1
Ripples and Dunes	683	N_L000_0683_ILT038CYL_S_1266_UNCORM1
Thinly Plated Outcrop	1093	N_L000_1093_ILT049CYL_S_2026_UNCORM1
Rough Platy Outcrop	1153	N_L000_1153_EDR050CYLTS_1624_DRIVEM1

Table 3
Navcam and Hazcam images for which elevation data were retrieved along traverses.

Sol	Terrain type	Product ID
29	*Smooth Plains*	NRA_400071695RADLF0040000NCAM00419M1
		NRA_400071053RADLF0040000NCAM00408M1
		NRA_400071081RADLF0040000NCAM00408M1
1093	*Irregular Sharp Outcrop*	NLB_494529821RADLF0492026NCAM00264M1
		RLB_494529071RADLF0492026RHAZ00311M1
1153	*Rough Platy Outcrop*	FLB_499848510RADLF0501222FHAZ00323M1
		RLB_499861454RADLF0501624RHAZ00313M1

The final unit is termed the *rough platy outcrop* and corresponds to Murray formation mudstones that have been eroded to more irregular surfaces as compared to *platy outcrop*, with some upturned plates composed of more resistant rock that stands above the more eroded mudstone plates (Fig. 17).

Wheel damage, as summarized in Section 4 of this paper, is associated with driving the wheels onto sharp objects due to the driving mode and suspension system. Thus the presence of sharp objects and the overall tilt distribution of the terrain both matter for determining damage rates. For example, a traverse with a significant roll would likely cause more damage than on a flat surface for the downhill wheels. Based on visual assessment of the various geomorphic units the most egregious terrain to cross would be the irregular sharp sandstone outcrops, followed by the *rough platy outcrop* units.

To quantify the assertions about geomorphic units and the potential for wheel damage vertical topographic profiles along traverses for several geomorphic units were retrieved from elevation maps generated from Navcam and Hazcam stereo images. Variograms are plots of topographic variance as a function of length scale and illustrate both the relative roughness of the geomorphic units and how each unit scales in terms of roughness as a function of length scale (e.g., Shepard et al., 2001) (Fig. 18). In addition, log-log linear fits to the data provide an indication of whether or not the terrains fit a single fractal dimension (through the Hurst exponent) and its associated magnitude. In fact, the *smooth plains* variogram is fit with a single Hurst exponent, with low topographic variances at all length scales (Fig. 18). The variogram for the *rough platy outcrop* shows that this unit is rougher than the *smooth plains* at all length scales and not well-fit by a single fractal dimension. The roughest unit is the *irregular sharp outcrop* at all length scales, including the finer-scales (centimeter to decimeter) that are likely to puncture and crack the wheels. In summary the variogram patterns are consistent with the inferences for mobility issues and wheel damage as summarized in this section of the paper and in the geomorphic unit descriptions given in Table 2.

6. Traverse planning and accumulated wheel damage

Given the mechanical understanding of wheel punctures and cracks propagation, an assessment and mapping of terrains and their likely impact on further wheel damage, drives were accomplished to avoid units with sharp embedded rocks. Surface properties scientists, science team members familiar with terrain properties, were embedded with mobility engineers on a tactical basis to make sure that the terrain maps were included in traverse planning, and that the most egregious obstacles were avoided. In addition, $-X$ direction drives were implemented more frequently (Fig. 19) to minimize additional damage to L1, L2, R1, and R2, until it was theorized that the wheel wear caused by the required post-drive turns in place to position the rover for end of drive imaging and telecommunications outweighed the benefits of $-X$ direction driving. This led to the decision to return to $+X$ direction drives as a baseline. The turns in place were thought to cause additional wheel damage, particularly to the middle wheels because they sweep the smallest radius arc during these maneuvers, creating elevated loads when engaging obstacles. When

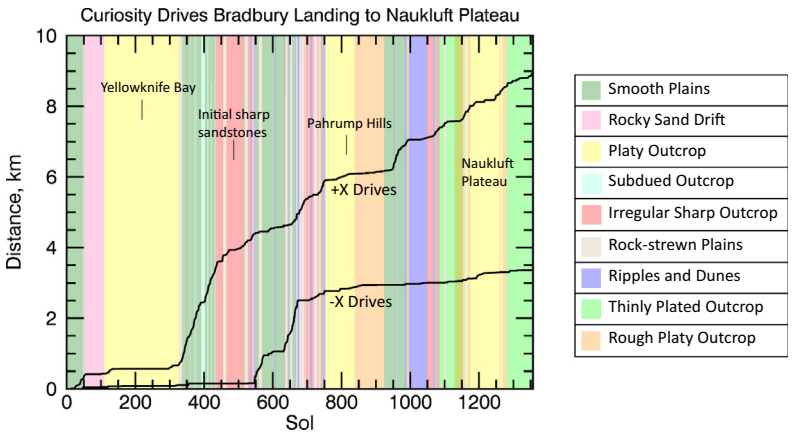

Fig. 19. **Cumulative distances for $+X$ and $-X$ drives as a function of sol**. The number of $-X$ drives increased starting on ~sol 550 when damage to the wheels was first observed. The rate was decreased on ~sol 700 when it was decided that turns in place at end of drive locations to position the rover for imaging for the next drive likely increased the probability of wheel damage. Geomorphic units traversed are shown in color-coded form. Note the increase in $-X$ drives after with initial encounters and associated wheel damage while traversing sharp sandstone outcrops. (For interpretation of the references to colour in this figure legend, the reader is referred to the web version of this article.)

traversing across surfaces likely to cause additional wheel damage the paths were carefully constructed to avoid the worst of the terrain elements and to minimize turns.

Even with careful traverse planning, informed by terrain unit mapping, additional wheel damage was expected to occur as traverse cumulative distance increased. For example, by sol 1315, near the edge of the Naukluft plateau (Figs. 1 and 8), punctures and cracks can be seen in both the L1 and L2 (Fig. 20). A useful metric to document damage is the total length of punctures and cracks as derived during MAHLI wheel imaging observations. Plots of cumulative crack lengths as a function of sol and distance traversed show a steady increase in damage (Fig. 21). As predicted from mechanical analysis and the dominance of $+X$ direction drives, L3 and R3 show the least amount of damage. L2 and R2 show the most damage, consistent with the high forces predicted while traversing over sharp obstacles. The large difference in damage between the L1 and R1 is not understood. It may be because the L1 was subjected to more damage when first encountering sharp sandstone outcrops, damage which then propagated quickly. This is evident in the rapid increase in cumulative tear lengths between the first and second MAHLI full wheel imaging stops (Fig. 21). A second increase in the rate of damage for L1 is evident at a traverse distance of ~9 km and is thought to be associated with rapidly propagating cracks while traversing the *platy outcrop* unit at Pahrump Hills. At the spatially detailed level, as compared to the mapping presented in Fig. 8, Pahrump Hills exhibits both *platy outcrop* and *rough platy outcrop* Murray formation exposures (Fig. 22). In addition parts of the Pahrump Hills mudstone outcrops are covered with small cobbles derived from weathering and downhill slope movement from capping sandstones. Curiosity also drove from outcrop to outcrop on the cobble-strewn mudstones because of the rich array of strata exposed. Note that the damage continued at a

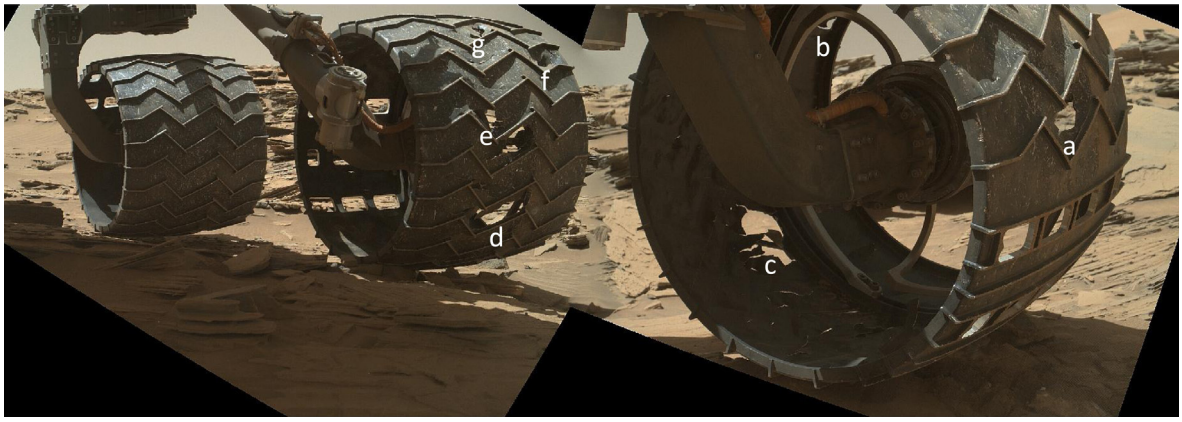

Fig. 20. **Mosaic of Curiosity left wheels taken on sol 1315.** MAHLI wheel image data for the left wheels acquired on sol 1315, with letters designating the larger punctures and tears. Compare to wheel images acquired on sols 84 (Fig. 2) and 488 (Fig. 4), which show less damage.

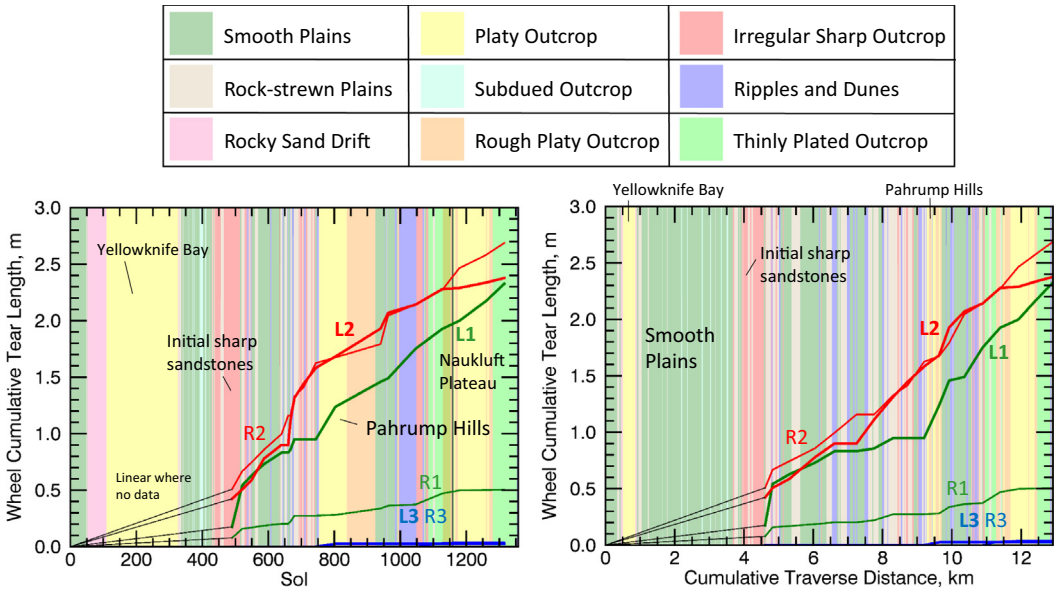

Fig. 21. **Cumulative wheel puncture and tear lengths as a function of sol and traverse distance.** Plots of cumulative wheel puncture and tear lengths (designated as cracks) as a function of sol (a) and traverse distance (b) for the six wheels, based on MAHLI full wheel imaging stops shown in Fig. 8. Note the enhanced L2 and R2 cumulative crack and the relatively small number on L3 and R3, a consequence of dominantly $+X$ driving and the mechanics of wheel-terrain interactions. As punctures and cracks increased the L1 and L2 total tear lengths approached one another, again because of the mechanics of wheel-terrain interactions. Note the increase in the rate of cumulative crack length/traverse distance for the L1 at the beginning of tracking the damage and again when in the Pahrump Hills. Simple linear interpolations are shown from landing to the beginning of tracking crack lengths.

Fig. 22. **Navcam mosaic of Pahrump Hills mudstone outcrops.** Navcam mosaic of a portion of the Pahrump Hills mudstone outcrops, with a partial wheel imprint in soil. These outcrops include both *platy outcrop* and *rough platy outcrop* units, with traverses across the latter likely associated with increased wheel L1 damage rates. Navcam product CX00826NL0442008F470821490VA.JPG.

higher rate after exiting Pahrump Hills, likely due to a combination of many pre-existing punctures and cracks, and traversing across rocky surfaces.

7. Wheel lifetime estimates and meeting mission science objectives

Curiosity's continued ascent on Mount Sharp will allow the rover to traverse to and conduct measurements on important science targets, including a ridge capped by hematite-bearing rocks, extensive outcrops with smectite exposures, and hydrated sulfate strata (Fig. 23). All of these rocks formed and/or were modified in the presence of water and the environments may have been habitable, i.e., they are key to meeting mission objectives focused on whether or not the red planet offered habitable environments (Grotzinger et al., 2012). Accessing these deposits does require traversing another dozen or more kilometers over rocky terrains and the key question is whether or not wheel damage would become so excessive that mobility would be hindered or made impossible. To better understand wheel lifetimes, the wheel anomaly investigation team focused considerable effort to construct half of a kinematically correct Curiosity suspension system, calibrated to produce reaction loads similar to the flight vehicle while operating continuously in the Mars Yard on a circular

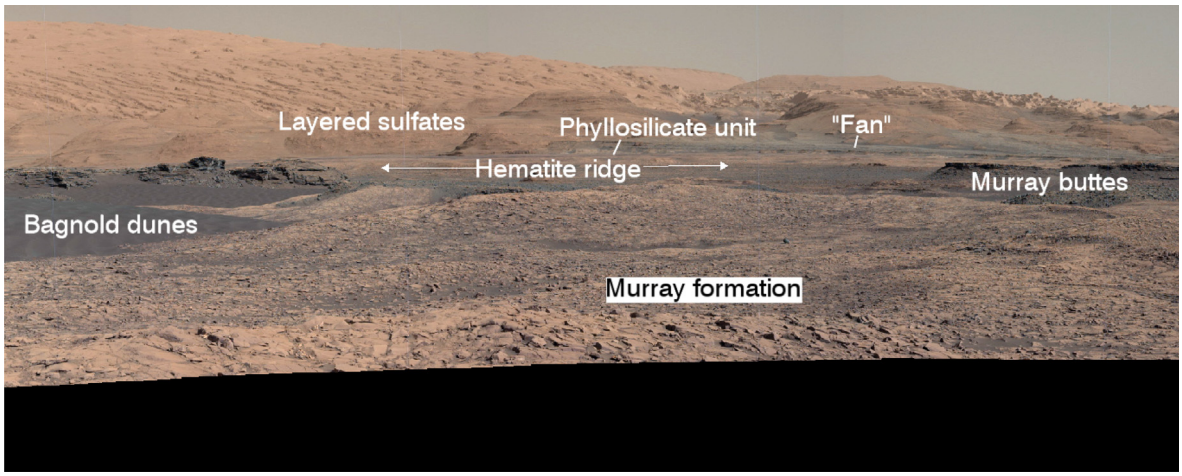

Fig. 23. **Mastcam color view of Mount Sharp.** Mastcam color view of Mount Sharp showing key strata that are targets for Curiosity investigations. Rough platy outcrop of Murray formation mudstones need to be traversed to get to a ridge capped by the mineral hematite and to the phyllosilicate and sulfate-bearing strata to the south. The "fan" is a geomorphic feature that is likely a continuation of the Stimson formation. Mosaic available from the Planetary Data System Geosciences Node Curiosity Analyst Notebook (http://pds-geosciences.wustl.edu/). (For interpretation of the references to colour in this figure legend, the reader is referred to the web version of this article.)

track simulating rocky terrains over distances needed to access the key strata to be encountered during the continued ascent of Mount Sharp. Results from this effort will be discussed in forthcoming publications and demonstrate that the wheels are highly likely to survive intact and provide the necessary traction for at least another ten or more kilometers, thereby allowing Curiosity to continue its ascent of Mount Sharp and to reach scientifically important strata.

8. Conclusions and implications

Curiosity landed on regolith-covered, rock-strewn plains to the north of Mount Sharp in August 2012. By June 2016 the rover had traversed 12.9 km to the southwest and the Naukluft Plateau, encountering extensive strata that were deposited in a fluvial-deltaic-lacustrine system. Highly fractured sandstone outcrops shaped by wind into sharp rock surfaces were evident on the plains as Curiosity traversed closer to the lower slopes of Mount Sharp, followed by similar sandstone outcrops that cap plateaus, with intervening valleys exposing mudstones variably covered with regolith and wind-blown sands. Differential wind erosion and scarp retreat are responsible for shaping these landforms, producing rough outcrops with sharp rock surfaces on the sandstone deposits. Initial drives across these rough surfaces were found to produce an unacceptably high rate of punctures in the 0.75 mm thick aluminum wheel skins.

Initial wheel damage observations led to an effort to produce a geomorphic map informed by the geologic setting and designed to assist in planning traverses that would minimize further wheel damage. Experiments and modeling efforts showed that the wheel static loads would not cause initial punctures or cracks. Rather initial damage was due to the mode of driving with the rocker-bogie suspension and six wheel drive actuator system in which wheels operating on leading arms are forced onto rocks by the other wheels as they maintained constant commanded angular velocities. Tracking wheel damage using Curiosity's imaging instruments showed an increase in crack propagation between landing in August 2012 and June 2016, in part because of drives across the irregular, sharp sandstone outcrops that could not be avoided.

Wheel lifetime estimates using experiments and analysis show that with careful path planning the wheels will be operational for an additional ten kilometers or more, thereby allowing the rover to reach and characterize the strata exposed on the slopes of Mount Sharp. This includes what is predicted from orbital observations to contain hematite, smectites, and hydrated sulfates formed in a variety of aqueous environments.

The NASA Mars 2020 rover will use the Curiosity rover and suspension design, but with re-designed wheels focused on increasing durability in sharp outcrops while maintaining or improving tractive performance in cohesionless sand-dominated dunes and ripples. The key objective for the Mars 2020 rover will focus on surface-based studies of the Martian environment, seeking preserved signs of biosignatures in rock samples that formed in ancient Martian environments with conditions that might have been favorable to microbial life. It is the first rover mission designed to seek signs of past microbial life (see Mars 2020 website, http://mars.nasa.gov/mars2020/, for source). Given the wheel damage issues associated with Curiosity's traverses across rocky terrains, and given that likely landing sites for the Mars 2020 rover will include rocky terrains, wheel re-design is underway. The Mars 2020 wheels will likely remain rigid, but will be made from a different aluminum alloy forged using the latest ring forging techniques, thereby removing stress concentrations. The

wheel diameters and skin thicknesses will be greater than those for the Curiosity rover. In addition, the wheel widths will be slightly smaller and there will be more grousers, redesigned to increase thrust relative to the Curiosity grousers. Historic overly simplified design guidelines such as use of engineering ground pressure have been superseded by systematic terramechanic design approaches, with a high importance placed on controlled single-wheel and vehicle level tests to assess tractive performance. The Mars 2020 program has also developed a terrain specification for wheel life testing that is more demanding than historic wheel life test terrains and conservatively represents the most challenging geologic units observed during Curiosity's traverse. Early testing of the Mars 2020 baseline wheel indicates durability will be substantially improved over even egregious terrain and that the Mars 2020 rover will have increased tractive performance in cohesionless material. Rover engineers are also developing an improved drive control algorithm which uses suspension pivot angular position data to estimate wheel-to-obstacle contact angles and correspondingly vary drive actuator output velocity with the objective of reducing suspension loads.

Acknowledgements

We thank the Mars Exploration Program, Mars Science Laboratory (Curiosity rover mission), and MSL wheel anomaly investigation team led by Richard Rainen for supporting the work presented in this paper. We thank the Geomorphic Mapping and Analysis Team, led by co-author John Grotzinger, for their tactical mapping and terrain analysis. We also thank the many engineers and scientists associated with the Curiosity mission who have helped in one way or another to make the mission a success and provided detailed reviews of this paper. We thank Fred Calef, JPL, for extensive work on HiRISE mosaic generation and co-registration with digital elevation maps generated from HiRISE stereo pair images. Funding was provided by NASA/Caltech/Jet Propulsion Laboratory to relevant institutions for participation in the Mars Science Laboratory (Curiosity) Mission. Part of this research was carried out at the Jet Propulsion Laboratory, California Institute of Technology, under a contract with the National Aeronautics and Space Administration.

References

Arvidson, R.E., Gooding, J.L., Moore, H., 1989. The Martian surface as imaged, sampled, and analyzed by the Viking Landers. Rev. Geophys. 27, 39–60. http://dx.doi.org/10.1029/RG027i001p00039.

Arvidson, R.E., Belutta, P., Calef, F., Fraeman, A.A., Garvin, J., Gasnault, O., Grant, J., Grotzinger, J., Hamilton, V., Heverly, M., Iagnemma, K.A., Johnson, J., Lanza, N., Le Mouélic, S., Mangold, N., Ming, D., Mehta, M., Morris, R.V., Newsom, H., Renno, N., Rubin, D., Schieber, J., Sletten, R., Vasavada, A.R., Vizcaino, J., Wiens, R.C., 2014. Terrain physical properties derived from orbital data and the first 360 sols of Mars Science Laboratory Curiosity rover observations in Gale Crater. J. Geophys. Res. E Planets 119, 1322–1344. http://dx.doi.org/10.1002/2013JE004605.

Arvidson, R.E., Iagnemma, K., Maimone, M., Fraeman, A., Zhou, F., Heverly, M., Bellutta, P., Rubin, D., Stein, N., Grotzinger, J., Vasavada, A., 2016. Mars Science Laboratory Curiosity megaripple crossings up to sol 710 in Gale Crater. J. Field Robot. http://dx.doi.org/10.1002/rob.21647.

Banham, S.G., Gupta, S., Rubin, D.M., Watkins, J.A., Sumner, D.Y., Grotzinger, J.P., Lewis, K.W., Edgett, K.S., Edgar, L.A., Stack, K.M., 2016. Reconstruction of an ancient eolian dune field at Gale Crater. In: Mars. 47th Lunar and Planetary Science Conference. Abstract 2346. pdf.

Bickler, D.B., 1988. Articulated Suspension System. United States Patent US 4840394 A.

Christensen, P., Jakosky, B., Kieffer, H., Malin, M., McSween Jr., H., Nealson, K., et al, 2004. The thermal emission imaging system (THEMIS) for the Mars 2001 Odyssey Mission. In: Russell, C. (Ed.), 2001 Mars Odyssey. Springer, Netherlands, pp. 85–130.

Edgett, K.S., Yingst, R.A., Ravine, M.A., Caplinger, M.A., Maki, J.N., Ghaemi, F.T., Schaffner, J.A., Bell III, J.F., Edwards, L.J., Herkenhoff, K.E., Heydari, E., Kah, L.C., Lemmon, M.T., Minitti, M.E., Olson, T.S., Parker, T.J., Rowland, S.K., Schieber, J., Sullivan, R.J., Sumner, D.W., Thomas, P.C., Jensen, E.H., Simmonds, J.J., Sengstacken, A.J., Willson, R.G., Goetz, W., 2012. Curiosity's Mars hand lens imager (MAHLI) investigation. Space Sci. Rev. 170, 259–317. http://dx.doi.org/10.1007/s11214-012-9910-4.

Grotzinger, J.P., Crisp, J., Vasavada, A.R., Anderson, R.C., Baker, C.J., Barry, R., Blake, D.F., Conrad, P., Edgett, K.S., Ferdowski, B., Gellert, R., Gilbert, J.B., Golombek, M., Gómez-Elvira, J., Hassler, D. M., Jandura, L., Litvak, M., Mahaffy, P., Maki, J., Meyer, M., Malin, M.C., Mitrofanov, I., Simmonds, J.J., Vaniman, D., Welch, R.V., Wiens, R.C., 2012. Mars Science Laboratory mission and science investigation. Space Sci. Rev. 170, 5–56. http://dx.doi.org/10.1007/s11214-012-9892-2.

Grotzinger, J.P., Gupta, S., Malin, M.C., Rubin, D.M., Schieber, J., Siebach, K., Sumner, D.Y., Stack, K.M., Vasavada, A.R., Arvidson, R.E., Calef, F., Edgar, L., Fischer, W.F., Grant, J.A., Griffes, J., Kah, L.C., Lamb, M.P., Lewis, K.W., Mangold, N., Minitti, M.E., Palucis, M., Rice, M., Williams, R.M.E., Yingst, R.A., Blake, D., Blaney, D., Conrad, P., Crisp, J., Dietrich, W.E., Dromart, G., Edgett, K.S., Ewing, R.C., Gellert, R., Hurowitz, J.A., Kocurek, G., Mahaffy, P., McBride, M.J., McLennan, S.M., Mischna, M., Ming, D., Milliken, R., Newsom, H., Oehler, D., Parker, T.J., Vaniman, D., Wiens, R.C., Wilson, S.A., 2015. Deposition, exhumation, and paleoclimate of an ancient lake deposit, Gale Crater, Mars. Science 350 (6257). http://dx.doi.org/10.1126/science.aac7575.

Haggert, S., Waydo, J., 2008. The mobility system wheel design for NASA's Mars Science Laboratory Mission. In: 11th European International Society Terrain Vehicle Systems Meeting, Torino, Italy.

Heverly, M., Matthews, J., Lin, J., Fuller, D., Maimone, M., Biesiadecki, J., Leighty, J., 2013. Traverse performance characterization for the Mars Science Laboratory Rover. J. Field Robot. 30 (6), 835–846. http://dx.doi.org/10.1002/rob.21481.

Maimone, M., Cheng, Y., Matthies, L., 2007. Two years of visual odometry on the Mars Exploration Rovers. J. Field Robot. 24 (3), 169–186. http://dx.doi.org/10.1002/rob.20184.

Maki, J., Theissen, D., Pourangi, A., Kobzeff, P., Litwin, T., Scherr, L., Eliott, S., Dingizian, A., Maimone, M., 2012. The Mars Science Laboratory engineering cameras. Space Sci. Rev. 170, 77–93. http://dx.doi.org/10.1007/s11214-012-9882-4.

Malin, M.C., Caplinger, M.A., Edgett, K.S., Ghaemi, F.T., Ravine, M.A., Schaffner, J.A., Baker, J.M., Bardis, J.D., DiBiase, D.R., Maki, J.N., Willson, R.G., Bell III, J.F., Dietrich, W.E., Edwards, L.J., Hallet, B., Herkenhoff, K.E., Heydari, E., Kah, L.C., Lemmon, M.T., Minitti, M. E., Olson, T.S., Parker, T.J., Rowland, S.K., Schieber, J., Sullivan, R. J., Sumner, D.Y., Thomas, P.C., Yingst, R.A., 2010. The Mars Science Laboratory (MSL) mast-mounted cameras (Mastcams) flight instru-

ments. In: 41st Lunar and Planetary Science Conference. Abstract 1123.pdf.

McEwen, A.S., Eliason, E.M., Bergstrom, J.W., Bridges, N.T., Hansen, C. J., Delamere, W.A., Grant, J.A., Gulick, V.C., Herkenhoff, K.E., Keszthelyi, L., Kirk, R.L., Mellon, M.T., Squyres, S.W., Thomas, N., Weitz, C.M., 2007. Mars reconnaissance orbiter's high resolution imaging science experiment (HiRISE). J. Geophys. Res. E Planets 112 (E5). http://dx.doi.org/10.1029/2005JE002605.

Moore, H.J., 1987. Physical properties of the surface materials at the Viking Landing sites on Mars. United States Geological Survey Professional Paper 1389, 222p.

Shepard, M.K., Campbell, B.A., Bulmer, M.H., Farr, T.G., Gaddis, L.R., Plaut, J.J., 2001. The roughness of natural terrain: a planetary and remote sensing perspective. J. Geophys. Res. 106, E32777–32795. http://dx.doi.org/10.1029/2000JE001429.

Vasavada, R., Chen, A., Calef, F.J., Crisp, J.A., Grotzinger, J.P., Arvidson, R.E., 2014. Overview of the Mars Science Laboratory mission: Earth to Bradbury Landing and Yellowknife Bay. J. Geophys. Res. E Planets 119. http://dx.doi.org/10.1002/2014JE004622.

Williams, R., Grotzinger, J., Dietrich, W., Gupta, S., Sumner, D., Wiens, R., Mangold, N., Malin, M.C., Edgett, K.S., Maurice, S., Forni, O., Gasnault, O., Ollila, A., Newsom, H.E., Dromart, G., Palucis, M.C., Yingst, R.A., Anderson, R.B., Herkenhoff, K.E., Le Mouélic, S., Goetz, W., Madsen, M.B., Koefoed, A., Jensen, J.K., Bridges, J.C., Schwenzer, S.P., Lewis, K.W., Stack, K.M., Rubin, D., Kah, L.C., Bell III, J.F., Farmer, J.D., Sullivan, R., Van Beek, T., Blaney, D.L., Pariser, O., Deen, R.G., Science Team, M.S.L., 2013. Martian fluvial conglomerates at Gale Crater. Science 340. http://dx.doi.org/10.1126/science.1237317.

Zhou, F., Arvidson, R.E., Bennett, K., Trease, B., Lindemann, R., Bellutta, P., Iagnemma, K., Senatore, C., 2014. Simulations of Mars rover traverses. J. Field Robot. 31, 141–160. http://dx.doi.org/10.1002/rob.21483.